Chapter 9
State-of-the-Art Medical Image Registration Methodologies: A Survey

Fahmi Khalifa, Garth M. Beache, Georgy Gimel'farb, Jasjit S. Suri, and Ayman El-Baz

Abstract Almost all computer vision applications, from remote sensing and cartography to medical imaging and biometrics, use image registration or alignment techniques that establish spatial correspondence (one-to-one mapping) between two or more images. These images depict either one planar (2-D) or volumetric (3-D) scene or several such scenes and can be taken at different times, from various viewpoints, and/or by multiple sensors. In medical image processing and analysis, the image registration is instrumental for clinical diagnosis and therapy planning, e.g., to follow disease progression and/or response to treatment, or integrate information from different sources/modalities to form more detailed descriptions of anatomical objects-of-interest. The unified registration goal – aligning a 2-D or 3-D target (sensed) image with a reference image – is reached by specifying a mathematical model of image transformations for and determining model parameters of the desired alignment. Frequently, the parameters provide an optimum of a goal function supported by the parameter space, so that the registration reduces to a certain optimization problem. This chapter overviews the 2-D and the 3-D medical image registration with special reference to the state-of-the-art robust techniques proposed for the last decade and discusses their advantages, drawbacks, and practical implementations.

Keywords Image registration · Similarity functions · Image transformations · Global registration · Nonrigid registration · Numerical optimization · Image resampling

A. El-Baz (✉)
BioImaging Laboratory, Department of Bioengineering, University of Louisville,
423 Lutz Hall Building, Louisville, KY, USA
e-mail: aselba01@louisville.edu

A. El-Baz et al. (eds.), *Multi Modality State-of-the-Art Medical Image Segmentation and Registration Methodologies: Volume 1*, DOI 10.1007/978-1-4419-8195-0_9,

9.1 Introduction

Image registration, sometimes called image alignment, mapping, or matching, establishes one-to-one spatial correspondence between two or more images of a single 2-D/3-D scene or several similar scenes captured (e.g., at different time instants, from various viewpoints, or by different sensors). This image processing step is fundamental in a variety of applications including remote sensing and cartography, autonomous navigation, robot vision, and medical imaging to mention a few. It is a powerful tool for integrating or fusing image data collected from different sensors (imaging modalities), tracking temporal evolution (changes in images taken at different times), making interpatient comparisons, reconstructing 3-D (volumetric) images from multiple 2-D (planar) images, etc. When one image is registered to another image, the latter is typically referred to as a *reference*, or prototype image, and the former – to be mapped onto the reference image – is called a *target*, sensed, source, or moving image.

Image registration in medical applications is instrumental for clinical diagnosis and therapy planning: e.g., if serial magnetic resonance imaging (MRI) scans of a particular patient, acquired over different time intervals, are to be compared in order to follow disease progression, response to treatment, or even dynamic structural change patterns of organ development [1]. Comparing the unregistered images can lead to incorrect diagnostic conclusions. Computer-aided diagnosis (CAD) systems use image registration to investigate how human anatomy is altering by disease, age, gender, handedness, and other clinical or genetic factors. Data fusion by registering images from various imaging sources (modalities), such as MRI, functional MRI (fMRI), computed tomography (CT), positron emission tomography (PET), single photon emission computed tomography (SPECT), and ultrasound (US) imagers, allows radiologists to base conclusions on the maximum amount of available information. Recently, image registration has opened up new medical imaging applications, namely, perfusion imaging and image-guided surgery [2].

The medical image registration techniques undergo continuous development and extensive research over the years and can be categorized according to various inherent properties such as similarity criteria, mapping models, optimization techniques, signal domains, image modalities, and so forth.

Similarity criteria in image registration are feature-based (also called geometric) or area/volume-based (intensity-based or iconic). The former account for salient points [3] or distinctive objects, such as closed contours [4], corners [5], etc., identified in an image. The correspondence between these features is established by measuring similarity between their quantitative descriptors. The area/volume-based criteria (e.g., [6, 7]) compare intensities (gray values), colors, or other pixel- or voxel-wise signatures directly, without feature extraction. Common hybrid registration techniques (e.g., [8–10]) combine advantages of both the classes.

Mapping or transformation models (functions) that establish spatial and signal relationships between the reference and target image domains make up two broad mapping classes: *rigid* (global) and *elastic* (nonrigid or local) transformations.

Most popular global geometric transformations include similarity, affine, perspective projection, and polynomial models. The affine transformations (e.g., [6, 11]) that account for translation, rotation, scaling, and skewness of a target with respect to a reference are sufficient, if the deformations of depicted anatomical structures are negligible relative to the required registration accuracy. However, the global mapping is unable to capture intrinsically local large deformations of anatomical structures. Thus, frequently more flexible elastic transformations (e.g., [12–25]) that locally warp a target to align with a reference image are needed. Most popular such transformations include radial basis functions (RBF), *physical continuum models* (viscous fluids), *and large deformation models* (diffeomorphisms).

Optimization techniques search for a local or global optimum of a cost (objective) function in the parameter space of the mapping model, the cost optimizer performing the goal registration. Local optimization (see, e.g., [26, 27]) is simpler than the global one but leads to accurate and robust registration only if the cost function is continuous and unimodal, which rarely appears in image registration. Otherwise, it converges to a close local optimum, causing misregistration unless good initial parameter values could be found [28]. Global optimization attempts to avoid local extrema that are common in many similarity criteria used as objective functions in medical image registration. Unfortunately, the global optimization algorithms, if they exist, typically converge too slow to the desired optimum and have too high computational loads. Some popular global optimization methods, e.g., genetic algorithm (GA) [29], simulated annealing (SA) [30], and particle swarm optimization (PSO) [31], perform a controllable stochastic search in the parameter space.

Spatial signal domain is used by a vast majority of image registration methods that match intensity patterns [6, 7], features [3, 4], or structures [11]. *Spatial Fourier frequency domain* (e.g., [32–45]) allows for a computationally more efficient search for some geometric transformations of a target image with respect to a reference image. In particular, a simple translation can be recovered in the frequency domain by applying the fast Fourier transform to the images and using phase correlation (PC) [33] or wavelet-based methods (e.g., [46]). More complicated methods such as [38] are used for finding both the translation and rotation. The advantage of the frequency domain is that the computed mapping parameters are relatively stable under various image artifacts, and the rotation and scaling can be determined independently of translation [47]. Typical spatial domain registration methods determine the rotation, scaling, and translation parameters simultaneously, often at the cost of their lower precision. However, a variety of transformations that can be estimated in the frequency domain is very limited [48].

Many registration algorithms assume only a single *image modality*, i.e., sensors of the same type. The *multimodality* algorithms register images captured by different imaging devices, typical examples include CT/MRI images [49], PET/CT images for tumor localization [13], original and contrast-enhanced CT images to segment-specific anatomic parts [50], MRI/PET images [51], and US/CT images [52].

Many further ways of classifying the registration methods exist, e.g., by data dimensionality (i.e., 2-D/2-D, 2-D/3-D, or 3-D/3-D registration), subjects involved (i.e., intrasubject, intersubject, or atlas-based registration), computational loads, and application areas (e.g., change detection or tumor monitoring). Due to diverse applications, scenes, and objects, a generic registration technique (and in particular a generic medical image registration technique) does not exist [3].

The medical image registration remains the challenging problem for many reasons. Physical relationships between the target and reference images are often difficult to model due to the highly nonrigid transformations involved. Also, one-to-one correspondence between the images may not exist due to missing or partial data. Furthermore, each imaging modality provides different information about a scene and introduces its own unique challenges [53]. Moreover, aligning images of different resolution with non-isotropic pixel or voxel dimensions may lead to excessive distortions. In addition, the depicted properties of the same objects in multiple images may considerably differ (e.g., large intensity differences for the same tissues, bones, fluids, or lesions). Finally, intrapatient, interpatient, and atlas-to-patient registrations offer extra challenges, and so on. Therefore, fast, robust, and efficient registration techniques are still in need (see e.g., comprehensive surveys [1, 2, 54–59] both in general purpose [54, 59] and medical image registration [1, 2, 55–58]) This chapter overviews in brief most popular 2-D and 3-D image registration techniques with special reference to the up-to-date medical image registration. Section 9.2 below details basic aspects of medical image registration including popular similarity functions, transformation models, image resampling, and optimization methods. Some of the recent state-of-the-art medical image registration techniques are reviewed in Sect. 9.3, and Sect. 9.4 presents the conclusions. The list of the symbols that are used throughout this chapter is given in Appendix A.

9.2 Image Registration Framework

The registration establishes correspondence between a reference image, I_r, and a target, I_t, by a parametric transformation, $T_\mathrm{g}(\cdot)$, of image geometry and signals or features in line with a similarity (or cost) function, $\rho(\cdot)$, specifying the registration accuracy. The optimal transformation maximizes the similarity (minimizes the cost):

$$T^*_\mathrm{g}(\cdot) = \arg\max_{T_\mathrm{g}(\cdot)} \rho(I_\mathrm{r}, T_\mathrm{g}(I_\mathrm{t})) \tag{9.1}$$

The optimization in (9.1) is mostly numerical. Starting from an initial guess, it is converging to the optimum in a series of iterative steps that depend on the objective (similarity) function, image transformations including resampling of a transformed image and optimization technique [54, 57, 59].

9.2.1 Similarity Functions

Similarity (cost) functions or measures quantify signal/feature correspondences between the target and reference images to guide the registration. The choice of a feature- or area-based function [59] depends generally on the application. The feature-based registration establishes one-to-one correspondence between distinctive features such as specific points [17, 60], contours [4], curves [5, 61–63], or surfaces [64–66] in both images. These features are usually represented by representative, or control points, e.g., gravity centers, line endings, etc., and the registration quality is determined by the accuracy of their correspondences.

The most popular scale-invariant feature transform (SIFT) by Lowe [67] reliably determines multiple point-wise correspondences between local areas differing in one image from another by the affine geometric and contrast/offset signal transformations. An intrasubject SIFT registration of retinal images collected with the 1-day time difference is exemplified in Fig. 9.1. Many other feature descriptors and similarity functions using their spatial relations to establish the point-wise correspondence between the target and reference images can be found in the comprehensive review [59]. Performance of the feature-based registration depends on many factors including, e.g., areas of overlaps between the images, severity of geometric distortions, noise, blurring and other signal (photometric) distortions, and similarities between dominant uniform (smooth) or textured image areas [68].

The area/volume-based registration matches directly pixel/voxel intensities [69] or colors or other sensed signals. While being known for a long time [70], it recently became the most popular method in the medical image registration (see, e.g., [12, 71–79]) due to no data losses from feature detection and no or little user interaction. In most cases, it is fully automated and allows for both qualitative and quantitative

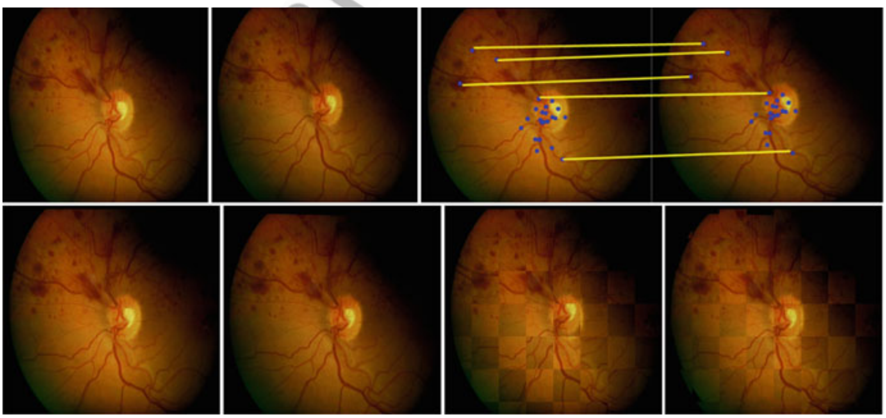

Fig. 9.1 SIFT-based retinal image registration: from *left* to *right* in the *upper row* – the reference image, target image, and candidate pixels for registration; in the *bottom row* – the reference image, the registered image, and the checkerboard visualization of the superposed target and reference before and after the registration

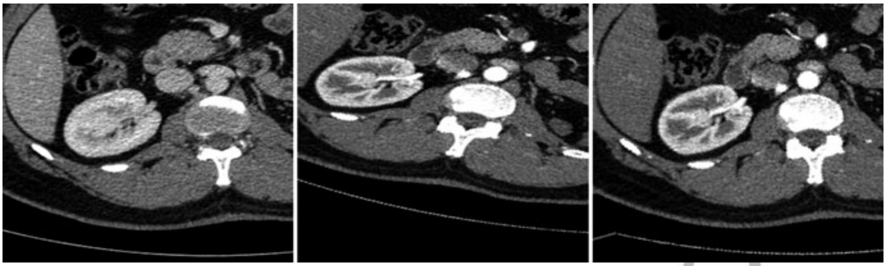

Fig. 9.2 An example of area-based registration: from *left* to *right* – the reference, target, and registered target CT kidney images

assessment of the alignment accuracy. Typically, the similarity function and optimal estimates of transformation parameters are derived from a probability model of the allowable transformation of a whole target or its predefined subregion (window) to a reference one. These techniques can efficiently align images of the same or different modality or dimensionality, accommodate rigid and elastic geometric deformations, and provide subpixel (voxel) accuracy [71, 80]. The area-based registration of intersubject CT kidney images by maximizing their mutual information [6] as the similarity measure is exemplified in Fig. 9.2.

The feature-based registration is highly effective in remote sensing, robotic vision, and other applications where distinctive and detectable structural image features exist. Because medical images are less rich with such structures, the area-based registration is also a viable alternative [59, 69] in spite of the higher computational complexity and more frequent local minima traps in optimization compared with the feature-based methods [5]. Well-known examples of similarity functions are the sum of squared differences (SSD) and ratio–image uniformity (RIU) [81], cross-correlation (CC) [61], phase correlation (PC) [33] (based on the Fourier shift theorem [83]), mutual information (MI) [6], and normalized mutual information (NMI) [82]. The SSD and CC are common for registering images of the same modality, while the MI and NMI are suitable for multiple modalities, too.

Cross-correlation (CC) is a basic similarity measure for registration [84–90] and template matching [91, 92] in classical signal/image processing, pattern recognition, and computer vision. For image registration, it is derived from a simple probabilistic model of target-to-reference image transformations of continuous, by assumption, scalar image signals:

$$I_{\mathrm{r}}(\mathbf{p}) = \mu I_{\mathrm{t}}(\mathbf{p}') + \delta + \Gamma(\mathbf{p}) \tag{9.2}$$

where $\mathbf{p}$ denotes a 2-D, $\mathbf{p} = (x, y)$, or 3-D, $\mathbf{p} = (x, y, z)$, point of the reference image, $\mathbf{p}'$ is the corresponding target point under a geometric transformation $\mathbf{p}' = T_{\mathrm{g}}(\mathbf{p})$, $I_{\mathrm{t}}(\mathbf{p}')$ and $I_{\mathrm{r}}(\mathbf{p})$ denote signals (intensities) in these points, μ and δ specify, respectively, an arbitrary global contrast and the offset deviation of the reference from the target, and $\Gamma(\mathbf{p})$ is a pixel/voxel-wise random noise with a center-symmetric (e.g., normal or Gaussian) probability density. The normalized CC for this model is invariant to the contrast/offset transformations of the target:

$$\mathrm{CC}_{T_{\mathrm{g}}(\cdot)}(I_{\mathrm{t}}, I_{\mathrm{r}}) = \frac{\sum_{\mathbf{p}\in\mathbf{W}} [I_{\mathrm{t}}(T_{\mathrm{g}}(\mathbf{p})) - \bar{I}_{\mathrm{t}}][I_r(\mathbf{p}) - \bar{I}_r]}{\sqrt{\left(\sum_{\mathbf{p}\in\mathbf{W}} [I_t(T_{\mathrm{g}}(\mathbf{p})) - \bar{I}_{\mathrm{t}}]^2\right)\left(\sum_{\mathbf{p}\in\mathbf{W}} [I_{\mathrm{r}}(\mathbf{p}) - \bar{I}_{\mathrm{r}}]^2\right)}} \tag{9.3}$$

where $\mathbf{W}$ denotes a window (usually, rectangular and chosen manually) in the reference image to be mapped to the target and $\bar{I}_{\mathrm{r}}$ and $\bar{I}_{\mathrm{t}}$ are mean values over the window for the reference and target image, respectively. To align the images, the maximum normalized CC is searched for in the parameter space of $T_{\mathrm{g}}(\cdot)$. The CC of (9.3) is in the range $[-1 \quad 1]$: the values close to 1 indicate strong matches between the images. (CC = 1 is the exact match.) When the geometric transformation is limited only to translations, $T_{\mathrm{g}}(\mathbf{p}) = \mathbf{p} - \delta$, e.g., $T_{\mathrm{g}}(x, y) = (x - \delta_x, y - \delta_y)$ or $T_{\mathrm{g}}(x, y, z) = (x - \delta_x, y - \delta_y, z - \delta_z)$, the coordinates of the peak CC are usually determined by direct exhaustion of the coordinate offsets δ between the two images. In more complex cases (e.g., an affine or projective transformation), the least squares CC or other generalized variants (see, e.g., [93]) are used so that the optimal transformation parameters are found by numerical optimization. The generalized CC can handle complex geometric transformations, but the computational load grows fast with the increasing numbers of parameters [94].

The normalized CC is a simple and effective similarity measure, and thus it is widely used in practice in spite of its non-robustness under spatially variant contrast and offset changes, e.g., due to varying illumination of complex 3-D surfaces and/or different sensor types. Moreover, two simpler cost measures, namely, SAD (sum of absolute differences) and SSD are frequently used for registering the reference and target images that are almost identical except for geometrical misalignment, i.e., have no contrast and offset deviations, $\mu = 1$ and $\delta = 0$ in (9.2) [95–103]:

$$\mathrm{SAD}(I_{\mathrm{t}}, I_{\mathrm{r}}) = \sum_{\mathbf{p}\in\mathbf{W}} |I_{\mathrm{r}}(\mathbf{p}) - I_{\mathrm{t}}(T_{\mathrm{g}}(\mathbf{p}))| \tag{9.4}$$

$$\mathrm{SSD}(I_{\mathrm{t}}, I_{\mathrm{r}}) = \sum_{\mathbf{p}\in\mathbf{W}} [I_{\mathrm{r}}(\mathbf{p}) - I_{\mathrm{t}}(T_{\mathrm{g}}(\mathbf{p}))]^2 \tag{9.5}$$

Close to zero SSD (or SAD) values indicate strong matches between the images (zero value gives the exact match). The SAD measure is more robust with respect to outliers or individual very large noise values in (9.2): large intensity changes in a small number of pixels (voxels) affect the SSD much more than the SAD. These cost functions are beneficial for certain medical images. For example, serial MRI or fMRI intrasubject scans are identical except for minor changes due to disease progression or response to treatment [102], so that in these cases the SAD and SSD are likely to work well. However, these measures are unsuitable in the presence of spatially uniform or variant contrast and offset deviations [103].

Fourier domain methods (e.g., [32–45]) transfer the classical CC registration from the image to the spatial frequency domain. The simple idea behind the resulting phase correlation (PC) method [33] is based on the Fourier shift property [83]: a constant shift between spatial coordinates of two functions $f_1(x, y)$ and $f_2(x, y)$, such that $f_2(x, y) = f_1(x - \delta_x, y - \delta_y)$, results in linear phase differences in the Fourier domain:

$$F_2(u, v) = F_1(u, v)\mathrm{e}^{-j(u\delta_x + v\delta_y)} \tag{9.6}$$

where $F_1(u, v) = \Im\{f_1(x, y)\}$ and $F_2(u, v) = \Im\{f_2(x, y)\}$ are the Fourier transforms of $f_1(x, y)$ and $f_2(x, y)$, respectively. Let $F_1^*(u, v)$denotes the complex conjugate of $F_1(u, v)$. Then, the PC of the functions f_1 and f_2 for all their mutual coordinate shifts can be restored by the inverse Fourier transform, $\mathrm{PC}_{f_1,f_2} = \Im^{-1}\{\mathrm{CPS}_{F_1,F_2}\}$, of the normalized cross-power spectrum:

$$\mathrm{CPS}_{F_1,F_2}(u, v) = \frac{F_2(u, v)F_1^*(u, v)}{|F_2(u, v)F_1^*(u, v)|} = \mathrm{e}^{-j(u\delta_x + v\delta_y)} \tag{9.7}$$

Then the simplest registration involving only translation has only to locate the PC peak in the spatial (δ_x, δ_y) coordinates. If $F_1(u, v)$ and $F_2(u, v)$ are continuous functions, then the inversed Fourier transform of $\mathrm{CPS}_{F_1,F_2}(u, v)$ is a delta function. The PC is of lower computational complexity than the usual CC when the fast Fourier transform (FFT) is employed to compute the spectra F_1 and F_2 for digital images. But the faster CC-based registration in the Fourier domain is simultaneously less accurate than in the signal domain and therefore it is more suitable for a coarse registration.

Foroosh et al. [36] and Shekarforoush et al. [43] have extended the PC to subpixel registration by analytic representation of down-sampled images. De Castro and Morandi [38] have extended it to more complicated registration scenarios combining both translation and rotation. Later, Reddy and Chatterji [34] improved the algorithm in [38] by reducing considerably the number of transformations needed. The Fourier–Mellin transform [34, 37, 39] and the cepstrum filter [40, 41] have been introduced to register images being misaligned by translation, rotation, and scaling. These approaches combine the PC with the log-polar transform (LPT). First, to recover translation, these methods apply a Fourier transform to images. Then, the LPT is applied to the magnitude spectrum, and the rotation and scale are recovered by phase correlation in the log-polar space [32]. A different approach by Zokai and Wolberg [44] performs the matching and localization in the spatial rather than frequency domain. The translation is recovered using the coarse-to-fine multiresolution framework, while the scale and rotation are obtained by matching the log-polar transformed images with the CC. Recently, Matungka et al. [45] proposed an adaptive polar transform (APT) combined with a projection transform to evenly and effectively sample an image in Cartesian coordinates. This approach requires less computations than the conventional LPT while remaining robust to both the scale and rotation changes. Due to low computational complexity and insensitivity to relative image translation, rotation, and scaling as well as to correlated pixel/voxel-wise noise and certain nonuniform signal variations, e.g., due to changing illumination, the PC is more appropriate in many practical applications than the classical CC [43].

Mutual information (MI) [6, 7] and normalized mutual information (NMI) [82, 104] are the most successful and commonly used universal and highly accurate similarity measures [105]. Recently, the MI has been shown to be efficient for aligning multimodal images [42, 106] and 2-D/3-D rigid and nonrigid registration [107]. The reference and target images are considered as a collection of statistically independent samples of a discrete random variable, and the MI and NMI evaluate the amount of information in a reference image about a target image (and vice versa) from statistical dependencies between the samples in the corresponding locations.

Let $\mathbf{X} = \{x_i, i = 1, \ldots, n\}$ and $\mathbf{Y} = \{y_j, j = 1, \ldots, m\}$ be finite signal sets for the reference and target image, respectively, and let $x'_i = \phi(x_i)$ and $y'_j = \psi(y_j)$ be one-to-one signal mappings: $\phi : \mathbf{X} \to \mathbf{X}' = \{x'_i, i = 1, \ldots, n\}$ and $\psi : \mathbf{Y} \to \mathbf{Y}' = \{y'_j, j = 1, \ldots, m\}$. Because the image signals are treated as independent samples, the MI and NMI functions are invariant both to arbitrary permutations of the corresponding locations $(\mathbf{p}, \mathbf{p}' = T_{\mathrm{g}}(\mathbf{p}))$ in the images and to arbitrary one-to-one mappings $(\phi; \psi)$ of their signal sets. Let p_i, q_i, and p_{ij} denote the (empirical) marginal probability of the target signal x_i, the reference signal y_i, and the corresponding pair (x_i, y_j), respectively: $p_i = P_{\mathrm{r}}(I_{\mathrm{r}}(\mathbf{p}) = x_i)$, $q_j = P_{\mathrm{r}}(I_{\mathrm{t}}(\mathbf{p}') = y_j)$, and $p_{ij} = P_{\mathrm{r}}(I_{\mathrm{r}}(\mathbf{p}) = x_i, I_{\mathrm{t}}(\mathbf{p}') = y_j)$, obtained by normalizing marginal and joint intensity histograms of the overlapping areas of I_{r} and I_{t}, respectively. Then the MI and NMI are defined as:

$$\mathrm{MI}(I_{\mathrm{r}}, I_{\mathrm{t}}) = H(I_{\mathrm{r}}) - H(I_{\mathrm{r}}|I_{\mathrm{t}}) = H(I_{\mathrm{t}}) - H(I_{\mathrm{t}}|I_{\mathrm{r}}) = \sum_{i=1}^{n}\sum_{j=1}^{m} p_{ij}\log\frac{p_{ij}}{p_i q_j} \quad (9.8)$$

$$\mathrm{NMI}(I_{\mathrm{r}}, I_{\mathrm{t}}) = \frac{H(I_{\mathrm{r}}) + H(I_{\mathrm{t}})}{H(I_{\mathrm{r}}, I_{\mathrm{t}})} = 1 + \frac{\mathrm{MI}(I_{\mathrm{r}}, I_{\mathrm{t}})}{H(I_{\mathrm{r}}, I_{\mathrm{t}})} \quad (9.9)$$

where $H(\cdot)$ is the Shannon's entropy $\left(H(I_{\mathrm{r}}) = -\sum_{i=1}^{n} p_i \log p_i, \quad \text{and } H(I_{\mathrm{t}}) = -\sum_{j=1}^{m} q_j \log q_j\right)$ of the signals, $H(\cdot,\cdot)$ is their joint entropy $\left(H(I_{\mathrm{r}}, I_{\mathrm{t}}) = -\sum_{i=1}^{n}\sum_{j=1}^{m} p_{ij}\log p_{ij}\right)$, and $H(\cdot|\cdot)$ is the conditional entropy $\left(H(I_{\mathrm{r}}|I_{\mathrm{t}}) = -\sum_{i=1}^{n}\sum_{j=1}^{m} p_{ij} \log p_{i|j} = -\sum_{i=1}^{n}\sum_{j=1}^{m} p_{ij}\log(p_{ij}/q_j)\right)$. The following obvious properties hold $H(I_{\mathrm{r}}) \geqslant H(I_{\mathrm{r}}|I_{\mathrm{t}}) \geqslant 0$, $H(I_{\mathrm{r}}, I_{\mathrm{t}}) = H(I_{\mathrm{r}}) + H(I_{\mathrm{r}}|I_{\mathrm{t}}) = H(I_{\mathrm{t}}) + H(I_{\mathrm{t}}|I_{\mathrm{r}})$, and $H(I_{\mathrm{r}}, I_{\mathrm{t}}) = H(I_{\mathrm{r}}) + H(I_{\mathrm{t}}) - H(I_{\mathrm{r}}|I_{\mathrm{t}})$

Image registration by minimizing the joint entropy was first proposed by Collignon et al. [108] and Studholme et al. [109]. However, this cost function was highly sensitive to the area of overlap between the images. To decrease the sensitivity, Viola [105] and Maes and Collignon [72] proposed to measure the MI and applied it to registering MRI and matching a 3-D object model to a real scene. Later, Studholme [104] proposed the NMI as a similarity measure that depends less on the overlap area and thus avoids misregistration. The MI and NMI generally work with the entire image data and directly with image intensities, but are rarely applied to points extracted from the area border as proposed by Rangarajan et al. [110]. Zhu [111] introduced the cross-entropy as an alternative information-based similarity measure. Comparisons between the MI and other information-based measures in the application to image registration can be found in [112].

Estimation of marginal and joint probabilities plays an important role in the MI/NMI-based image registration. Wells et al. [106] employed widely used nonparametric Parzen window estimates [113], whereas Maes and Collignon [72] employed conventional normalized joint histograms. Niu [114] improved the approach in [72] by using Kriging estimation (KE). The Parzen window-based estimates result in differentiable MI/NMI functions and corresponding optimization techniques. The histogram-based estimates lead to a derivative-less multivariate optimization (e.g., the Powell's direction set method [72]).

The MI/NMI-based registration is widely used in medical image analysis. However, it has a few drawbacks. The lack of signal (intensity) values in some images, i.e., lossy rather than one-to-one signal mapping, and the amount and distribution of image noise may heavily influence the registration accuracy. Also, the MI and NMI do not account for spatial relationships between adjacent pixels or voxels. To improve the MI/NMI-based registration by using spatial signal relationships, the MI is sometimes combined with the gradient information [74], or limited to within clusters of feature points [115], or combined with the correlative edge deviation [116].

Markov–-Gibbs random filed (MGRF)-based similarity measure proposed in [117, 118] is derived from an MGRF model of target images. The reference image is used as a training sample to learn a characteristic structure of pairwise pixel or voxel dependencies, called interactions, such as e.g., in Fig. 9.3, and Gibbs potential functions of signal co-occurrences on these pairs.

Let $\mathbf{N}$ denote a finite set of 2-D (or 3-D) coordinate offsets $\Delta = (\delta_x, \delta_y)$ (or $(\delta_x, \delta_y, \delta_z)$) defining a spatially uniform family of interacting pixel (voxel) pairs, called neighbors. Each pair of the neighbors is the second-order clique of an interaction graph with nodes in the pixels (voxels) and edges between the neighbors. The target-to-reference similarity in their overlap area $\mathbf{W}$ is measured by the relative Gibbs energy of pairwise target signal co-occurrences:

$$E(I_{\mathrm{t}}; \mathbf{W}) = \sum_{\Delta \in \mathbf{N}} \lambda_\Delta \mathbf{V}_\Delta^{\mathrm{T}} \mathbf{F}_\Delta(I_{\mathrm{t}}; \mathbf{W}) \equiv \sum_{\Delta \in \mathbf{N}} \lambda_\Delta \sum_{(y,y') \in \mathbf{Y}^2} V_\Delta(y, y') F_\Delta(y, y' | I_{\mathrm{t}}; \mathbf{W}) \quad (9.10)$$

Fig. 9.3 Characteristic pairwise voxel interaction in a 3-D MGRF image model

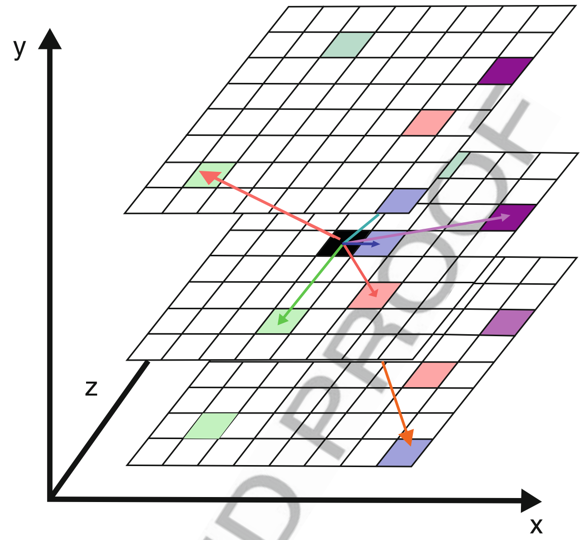

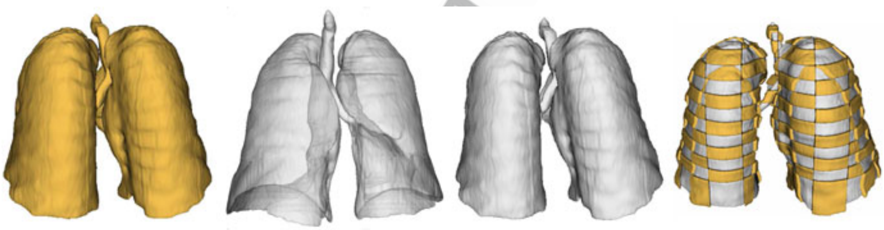

Fig. 9.4 MGRF-based 3-D image registration: from *left* to *right* – the reference, target images, the 3-D affine transformation of the target, and the checkerboard visualization of the co-aligned reference and transformed target

where $\mathbf{V}_\Delta = (V_\Delta(y, y') : (y, y') \in Y^2)$ is the learned potential function of signal co-occurrences over the second-order clique family with the inter-node coordinate offset $\boldsymbol{\Delta}$, λ_Δ is the relative cardinality of this family on the area $\mathbf{W}$, and $\mathbf{F}_\Delta(I_\mathrm{t}; \mathbf{W}) = (F_\Delta(y, y'|I_\mathrm{t}; \mathbf{W}) : (y, y') \in Y^2)$is the empirical probability of signal co-occurrences in this clique family on the area $\mathbf{W}$. The geometric transformation for aligning I_t with I_r maximizes the MGRF energy of (9.10). Experiments in global affine 3-D image registration [117, 118] using an automatic initialization followed by gradient search suggest that the MGRF similarity function aligns complex 2-D/3-D objects more accurately than more conventional popular measures. An example of the MGRF-based 3-D image registration is presented in Fig. 9.4.

Other similarity/cost measures in addition to the above most well-known ones have been proposed and applied successfully to different image registration problems, e.g., ratio–image uniformity (RIU) (also known as variation of intensity ratios) [119, 120], partitioned intensity uniformity (PIU) (also known as variance of intensity ratios) [51, 121–124], variance of gray values within segments [125, 126], histogram entropy of difference images [127], histogram clustering and dispersion [41, 108, 128], zero crossings in difference images [stochastic sign change (SSC) and deterministic sign change (DSC) criteria] [129–136], local low-order Taylor expansions determined by the image gray values [137], cepstral echo filtering [138], and optical flow field [139, 140]. However, some of these methods get good registration results only after complex image preprocessing to remove anatomic background and form the target and reference images including only the object pixels or voxels.

9.2.2 Geometric Transformations

Geometric mapping, or transformation $T_g(\cdot)$, relates the target plane or volume to the reference one, i.e., aligns or register the target to the reference to establish one-to-one correspondence between their pixels or voxels. Medical images always have nonuniform geometric differences (deformations) due to the nature of objects-of-interest and image acquisition including scanner-induced deformations, patient movements, surgical interventions, etc. The mapping model depends on the assumed target-to-reference deformations, required registration accuracy, and images to be registered [141].

All the mapping models fall into two basic categories: *rigid* (global) and *nonrigid* (elastic) transformations. The rigid models (see, e.g., [6, 11]) transform uniformly the whole 2-D or 3-D images, e.g., translate, rotate, scale, and/or shear every depicted object just in the same manner. While these models are sufficient in many applications, medical objects to be co-aligned always have spatially variant geometric differences. Such complex deformations of images suggest more flexible elastic models that register a target to a reference image by spatially variant local warping (see, e.g., [12–25]). Common global models include affine transformations, similarity transformations being a frequent particular case, and perspective projections. Sometimes more general polynomial transformations of the target 2-D area or 3-D volume[1] are also associated with the global models. Some examples of 2-D rigid transformations are shown in Fig. 9.5, and Fig. 9.6 demonstrates a very simple nonrigid transformation. Elastic models produce considerably more flexible image transformations by using, e.g., radial basis functions (RBF), physical continuum models (viscous fluids), or large deformation models (diffeomorphisms). A comprehensive analysis of the popular nonrigid transformations can be found in [142].

[1] For example, a quadratic 2-D mapping of target points $(x, y)$to reference points (x', y'): $x' = a_{00} + a_{10}x + a_{01}y + a_{20}x^2 + a_{02}y^2 + a_{03}xy$; $y' = b_{00} + b_{10}x + b_{01}y + b_{20}x^2 + b_{02}y^2 + b_{03}xy$; with 12 parameters a_{ij}, b_{ij}, to be estimated (e.g., from the six exact correspondences of the points).

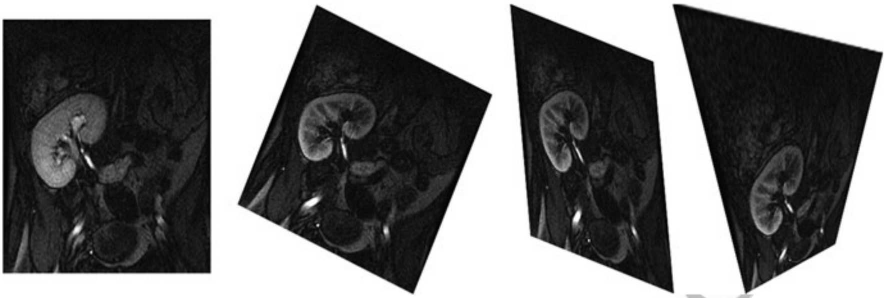

Fig. 9.5 Rigid transformation: from *left* to *right* – the reference image and similarity, affine, and projective transformations of the target image

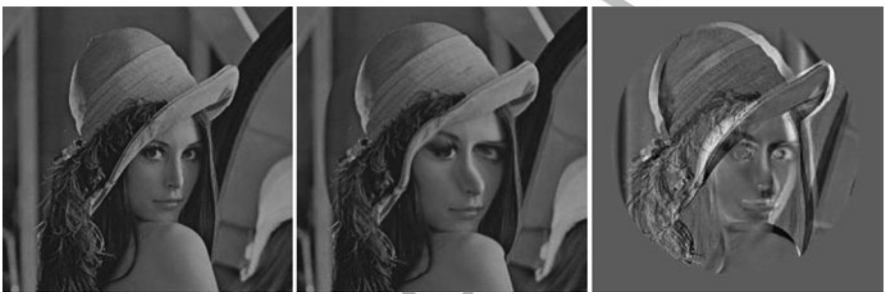

Fig. 9.6 Nonrigid transformation: from *left* to *right* – the initial, transformed, and difference images

Rigid or global transformations are conveniently converted into linear (matrix–vector) operations by using so-called *homogeneous* coordinates. Every Cartesian 2-D or 3-D point coordinates **p** produce an infinite set of the equivalent 3-D or 4-D, respectively, homogeneous coordinates p̃ such that the initial Cartesian coordinates are simple ratios of the homogeneous coordinates:

$$\text{if } \mathbf{p} = \begin{bmatrix} x \\ y \end{bmatrix} \text{ then } \tilde{\mathbf{p}} == \begin{bmatrix} \tilde{x} = \tau \cdot x \\ \tilde{y} = \tau \cdot y \\ \tau \end{bmatrix} \text{ and if } \mathbf{p} = \begin{bmatrix} x \\ y \\ z \end{bmatrix} \text{ then } \tilde{\mathbf{p}} == \begin{bmatrix} \tilde{x} = \tau \cdot x \\ \tilde{y} = \tau \cdot y \\ \tilde{z} = \tau \cdot z \\ \tau \end{bmatrix}$$

with an arbitrary scale coordinate τ, i.e., $x = \tilde{x}/\tau$, $y = \tilde{y}/\tau$, etc. The global 2-D translation by coordinate-wise steps δ_x and δ_y, rotation by θ, coordinate-wise scaling by factors α_x and α_y, and shearing by factors ζ_x and ζ_y are exemplified in Fig. 9.7.

An *Affine transformation* maps straight lines into straight lines while preserving properties of the lines to be parallel or intersect but not preserving neither lengths nor angles between the lines. Therefore, geometric objects change their shapes.

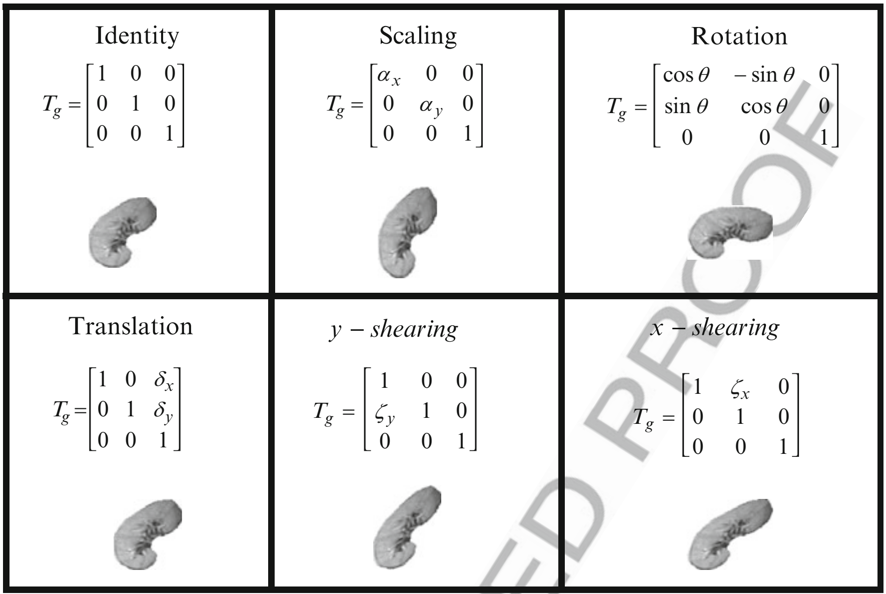

Fig. 9.7 Particular cases of a rigid 2-D affine transformation $\tilde{\mathbf{p}}' = \mathbf{T}_g \tilde{\mathbf{p}}$

A planar (2-D) affine transformation can be described by independent translation, rotation, scaling, and shearing (seven parameters in total):

$$\begin{aligned} \begin{bmatrix} \tilde{x}' \\ \tilde{y}' \\ 1 \end{bmatrix} &= \begin{bmatrix} a_{11} & a_{12} & a_{13} \\ a_{21} & a_{22} & a_{23} \\ 0 & 0 & 1 \end{bmatrix} \begin{bmatrix} \tilde{x} \\ \tilde{y} \\ 1 \end{bmatrix} \\ &\equiv \begin{bmatrix} 1 & 0 & \delta_x \\ 0 & 1 & \delta_y \\ 0 & 0 & 1 \end{bmatrix} \begin{bmatrix} \alpha_x & 0 & 0 \\ 0 & \alpha_y & 0 \\ 0 & 0 & 1 \end{bmatrix} \begin{bmatrix} \cos\theta & -\sin\theta & 0 \\ \sin\theta & \cos\theta & 0 \\ 0 & 0 & 1 \end{bmatrix} \\ &\quad \times \begin{bmatrix} 1 & 0 & 0 \\ \zeta_y & 1 & 0 \\ 0 & 0 & 1 \end{bmatrix} \begin{bmatrix} 1 & \zeta_x & 0 \\ 0 & 1 & 0 \\ 0 & 0 & 1 \end{bmatrix} \begin{bmatrix} \tilde{x} \\ \tilde{y} \\ 1 \end{bmatrix} \end{aligned} \tag{9.11}$$

The affine parameters are uniquely determined from the known coordinates of three corresponding pairs of points forming triangles to be co-aligned in the target and reference images. A 3-D affine transformation depends on the 12 parameters that can be determined from the known four corresponding pairs of points forming the tetrahedrons to be co-aligned in the images:

$$\begin{bmatrix} \tilde{x}' \\ \tilde{y}' \\ \tilde{z}' \\ 1 \end{bmatrix} = \begin{bmatrix} a_{11} & a_{12} & a_{13} & a_{14} \\ a_{21} & a_{22} & a_{23} & a_{24} \\ a_{31} & a_{32} & a_{33} & a_{34} \\ 0 & 0 & 0 & 1 \end{bmatrix} \begin{bmatrix} \tilde{x} \\ \tilde{y} \\ \tilde{z} \\ 1 \end{bmatrix} \tag{9.12}$$

Similarity transformation is a particular case of the affine transformation that preserves shapes of objects. It does not affect angles between lines while changing lengths of the lines and positions of points because it accounts for only translation, rotation, and uniform scaling $\alpha_x = \alpha_y = \alpha$. With the unit scale factor $\alpha = 1$ (i.e., with only translation and rotation), it is called the *orthogonal transformation*. The affine parameters for the 2-D similarity transformation ($a_{11} = \alpha \cos\theta$, $a_{12} = -\alpha \sin\theta$, $a_{13} = \delta_x$, $a_{21} = \alpha \sin\theta$; $a_{22} = -\alpha \cos\theta$, and $a_{23} = \delta_y$) depend on the four parameters (δ_x, δ_y, α, and θ) that can be determined from the known coordinates of two corresponding pairs of points in the images. The 3-D similarity transformation depends on seven parameters: three translations, three rotation angles, and one scaling factor. If the point-to-point correspondences are noisy or inaccurate, the affine parameters are determined from a large number of point-to-point correspondences by the least squares [143] or clustering [144] methods.

Perspective projection transformations also map lines to lines, but do not necessarily preserve their property to be parallel. Optical image acquisition performs an exact 3-D to 2-D projection, if the lens and sensor nonlinearities are not taken into account:

$$\begin{bmatrix} \tilde{x}' \\ \tilde{y}' \\ \tilde{z}' \end{bmatrix} = \begin{bmatrix} a_{11} & a_{12} & a_{13} & a_{14} \\ a_{21} & a_{22} & a_{23} & a_{24} \\ a_{31} & a_{32} & a_{33} & a_{34} \end{bmatrix} \begin{bmatrix} \tilde{x} \\ \tilde{y} \\ \tilde{z} \\ 1 \end{bmatrix} \tag{9.13}$$

When an almost flat frontal scene ($z \approx \text{const}$) is projected, the above relations between the 3-D (x, y, z) and 2-D (x, y) points: $x' = \frac{a_{11}x + a_{12}y + a_{13}z + a_{14}}{a_{31}x + a_{32}y + a_{33}z + a_{34}}$ and $y' = \frac{a_{21}x + a_{22}y + a_{23}z + a_{24}}{a_{31}x + a_{32}y + a_{33}z + a_{34}}$ can be simplified to $x' = \frac{b_{11}x + b_{12}y + b_{13}}{c_{11}x + c_{12}y + 1}$ and $y' = \frac{b_{21}x + b_{22}y + b_{23}}{c_{21}x + c_{22}y + 1}$.

Nonrigid or elastic transformations are needed when geometric differences between the target and reference images are spatially variant and global transformations become inadequate, i.e., errors of the rigid registration are too large and their probability distributions vary with the location [56, 59]. Medical image analysis frequently employs spline-based nonrigid mapping models including thin-plate splines (TPS) [15], elastic body splines (EBS) [17], and *cubic B-splines* [14].

TPS or surface splines [145, 146] are the most popular examples of using RBF to model spatially variant geometric deviations in image registration. Originally introduced by Goshtasby [147] in remote sensing, this mapping model was applied then by Grimson [148] and Bookstein [15] to medical images. At present, the TPS are widely used in medical image registration (see, e.g., [149–152]) to approximate a dense deviation field with a due balance between smoothness and accuracy of the registration. Given N control points $\{(x_k, y_k, f_k) : k = 1, 2, \ldots, N\}$ of a continuous 2-D function, $f(x, y)$, the TPS interpolates all the points as follows [142]:

$$f(x, y) = a_{00} + a_{10}x + a_{01}y + \sum_{k=1}^{N} F_k r_k^2 \ln(r_k^2) \tag{9.14}$$

where $r_k^2 = (x - x_k)^2 + (y - y_k)^2 + \eta^2$ is the augmented Cartesian distance between the points (x, y) and (x_k, y_k), the value η^2 acting as a stiffness parameter, and a_{00}, a_{10}, a_{01} and $F_k; k = 1, 2, \ldots, N$ are the numerical parameters determined by solving a system of $N + 3$ linear equations. This model describes deformations of an infinite plate under N loads causing fixed deflections at the control points. The latter provide N linear equations that come from (9.14) by letting $f(x_k, y_k) = f_k$, and the three more equations come from constraining the TPS to ensure that the plate will not translate or rotate:

$$\sum_{k=1}^{N} F_k = 0; \quad \sum_{k=1}^{N} x_k F_k = 0; \quad \sum_{k=1}^{N} y_k F_k = 0 \tag{9.15}$$

Due to combined affine and non-affine warping, the TPS captures both the global rigid and local nonrigid deviations and gives good registration accuracy. However, the number of parameters grows linearly with the number of control points, and computations become quickly time consuming. Considerable attention has been paid to decreasing the TPS complexity while keeping reasonable accuracy (see, e.g., [153–156]). A comprehensive study of the TPS-based registration of medical images can be found in [157]. The TPS is easily extended to 3-D images (e.g., [158]) by modifying (9.14):

$$f(x, y, z) = a_{000} + a_{100}x + a_{010}y + a_{001}z + \sum_{k=1}^{N} F_k r_k^2 \ln(r_k^2) \tag{9.16}$$

where $r_k^2 = (x - x_k)^2 + (y - y_k)^2 + (z - z_k)^2 + \eta^2$ and adding one more constraint:

$$\sum_{k=1}^{N} z_k F_k = 0 \tag{9.17}$$

An EBS was proposed in [17] for landmark-based registration of 3-D breast MRI. The EBS is a solution to the *Navier–Cauchy* PDE of linear elasticity describing the equilibrium displacements of a homogeneous, isotropic, and elastic material under a radially symmetric polynomial force. As was reported in [17], the EBS outperformed the TPS in the registration accuracy.

Cubic B-splines are the most widely used nonrigid free-form deformation (FFD) models. These spline models were introduced first by Sederberg and Parry [159] in computer graphics and used then by Rueckert et al. [14] for registering the breast MRI. In contrast to the TPS [15] and EBS [17], the locally controlled B-splines remain computationally efficient even for a very large number of control points. Because their basis functions have a limited support, any movement of a control point affects only a local neighborhood of that point. An FFD-based registration of the images in Fig. 9.6 is illustrated in Fig. 9.8.

Let $\Phi = (\Phi_{l,m} : l = 0, 1, \ldots, L - 1; m = 0, 1, \ldots, M - 1)$ denote a lattice of $L \times M$ control points $\Phi_{l,m}$ with uniform linear spacing γ. Let (x, y) denote the

Fig. 9.8 FFD registration: from *left* to *right* – the reference, target, the registered target, deformation field, and error images

Cartesian coordinates of planar points in the γ-units and let $\lfloor B \rfloor$ be the integer part of a real-valued number B. The FFD model is defined by the 2-D tensor product of standard uniform cubic 1-D B-splines $\beta_k(\cdot)$ [159]:

$$f(x,y) = \sum_{i=-1}^{2} \sum_{j=-1}^{2} \beta_i(s)\beta_j(t)\Phi_{l+i,m+j} \tag{9.18}$$

where $l = \lfloor x \rfloor$, $m = \lfloor y \rfloor$, $(s,t) : s = x - l \in [0,1)$, and $t = y - m \in [0,1)$ are the relative position of the point (x,y) with respect to the nearest lattice points (l,m), $(l+1,m)$, $(l,m+1)$, $(l+1,\, m+1)$, and $\beta_k(u)$ are the kth basis function, $u \in [0,1); k = -1,\ldots,2$, of the uniform cubic B-spline [160, 161]:

$$\begin{aligned} &\beta_{-1}(u) = \tfrac{1}{6}(-u^3 + 3u^2 - 3u + 1); \quad \beta_0(u) = \tfrac{1}{6}(3u^3 - 6u^2 + u) \\ &\beta_1(u) = \tfrac{1}{6}(-3u^3 + 3u^2 + 3u + 1); \quad \beta_2(u) = \tfrac{1}{6}u^3 \end{aligned} \tag{9.19}$$

The control points are the FFD parameters, and the resolution of the lattice Φ (or the mesh in the 3-D case) determines the number of the control points and therefore the computational complexity. The large lattice spacing γ permits the representation of nonrigid deviations of the whole image, whereas the fine lattice allows for modeling highly local nonrigid deviations. The 3-D FFD is represented by the 3-D tensor product of the same 1-D uniform cubic B-splines:

$$f(x,y,z) = \sum_{i=-1}^{2} \sum_{j=-1}^{2} \sum_{k=-1}^{2} \beta_i(s)\beta_j(t)\beta_k(w)\Phi_{l+i,m+j,n+k} \tag{9.20}$$

where $n = \lfloor z \rfloor$ and $w = z - n \in [0,1)$

The TPS, EPS, and cubic B-spline models yield an overall smooth image deformation but become problematic when desired local deformations have to be limited to only specific image parts. To cope with such deformations, the control points have to be well distributed over the image and prevent deformations in regions that should not be changed [162].

More flexible RBF-based models (e.g., [162, 163]) include special parameters into the basis functions to control the locality of deformations:

$$f(\mathbf{p}) = \sum_{k=1}^{N} F_k R_k(\mathbf{p}) \tag{9.21}$$

where $R_k(\mathbf{p})$ is a real-valued RBF depending on the distance $r_k(\mathbf{p}) = |\mathbf{p} - \mathbf{p}_k|$ between $\mathbf{p}$ and the control point $\mathbf{p}_k$, and F_k specifies the influence of this RBF onto the value $f(\mathbf{p})$ (here, the distance $r_k(\mathbf{p}) = \sqrt{(x-x_k)^2 + (y-y_k)^2}$ in the 2-D and $\sqrt{(x-x_k)^2 + (y-y_k)^2 + (z-z_k)^2}$ in the 3-D case). Typical examples are multiquadric (MQ), Gaussian, and inverse MQ-based RBF models with $R_k(\mathbf{p}) = (r_k^2(\mathbf{p}) + \eta^2)^{0.5}$, $\exp(-r_k^2(\mathbf{p})/(2\sigma_k^2))$, $(r_k^2(\mathbf{p}) + \eta^2)^{-0.5}$, respectively. The parameters $F_k : k = 1, 2, \ldots, N$ are estimated by letting $f(\mathbf{p}_k) = f_k$ for the control points $k = 1, 2, \ldots, N$.

The MQ-based RBF was investigated for both image registration [141] and deformation [163] largely influences locations being far off the control point $\mathbf{p}_k$. Conversely, the inverse MQ (e.g., [164]) and Gaussian RBFs (e.g., [162, 165, 166]) decrease their influence with the growing distance to the control point. Local properties of the TPS were compared with the Gaussian and MQ RBF models in [163]. Moreover, a comparative study by Franke [167] has found that monotonically decreasing RBFs perform worse than the monotonically increasing RBFs and the MQ followed by the TPS produced the best accuracy in interpolating randomly spaced data. An excellent review of the RBF models can be found in [168].

When only a fraction of the control points is used to find the value $f(\mathbf{p})$, the RBFs are called *compactly supported*. Wendland [169] described a family of compactly supported and positive definite RBFs such that the resulting system of equations is always solvable. Later Fornefett et al. [170] introduced an elastic registration using positive definite functions of compact support to align pre- and postoperative 2-D and 3-D tomographic images in the case of tumor resection. Image registration results with the globally defined RBFs and the compactly supported RBFs were compared in [171].

Many other efficient and sophisticated nonrigid registration techniques have been developed for various medical applications: see, e.g., [12–25]. Recently, El-Baz et al. [172] and Khalifa et al. [173] proposed to register a segmented target object to the reference one by accurate co-alignment of their conjugate internal closed contours. As shown in Fig. 9.9, a distance map is generated inside each object by finding for every inner point the closest distance to the object's boundary. The map is used to form a collection of separate, equispaced iso-contours within the object, the number of the contours depending generally on the required registration accuracy and speed. Correspondence between the target and reference iso-contours is evaluated by either their NCC (normalized cross-correlation) [172] or solving a special PDE [173]. In [172], the target iso-contours are evolved under a specific exponential speed function to fit the conjugate reference contours. In [173], the authors avoid using the exponential speed function by solving Laplace's PDE

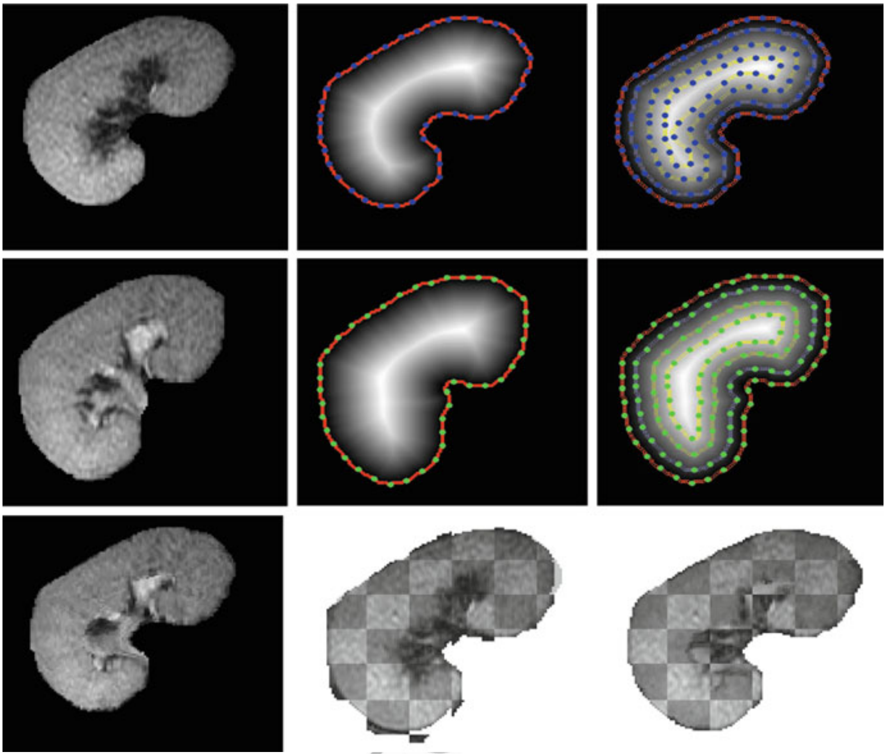

Fig. 9.9 Iso-contour-based kidney registration: from *left* to *right* in the *upper row* – the reference image, its distance map, and iso-contours; in the *middle row* – the target image, its distance map and iso-contours; in the *bottom row* – the aligned target and checkerboard visualization before and after the registration

between respective iso-contours. The solution of Laplace's equation results in intermediate equipotential surfaces (dashed lines in Fig. 9.10) and streamlines (filed lines) that connect both iso-contours (e.g., $\mathbf{P_A}$ and $\mathbf{P_B}$ in Fig. 9.10). These streamlines are defined as being everywhere orthogonal to all equipotential surfaces (e.g., the line connecting the points P_{ai} and P_{bj} in Fig. 9.10) and are used to find the point-to-point correspondences between both boundaries. Deforming a medical object by inner contours is more accurate than by deforming a lattice: see, e.g., Fig. 9.11 showing the application to the retinal images in Fig. 9.1.

9.2.3 Numerical Optimization

As shown in Sect. 9.2.1, cost or similarity functions for image registration are typically invariant to expected target-to-reference signal transformations due to the use of either specific functions (e.g., the MI or NMI) or explicit parametric signal

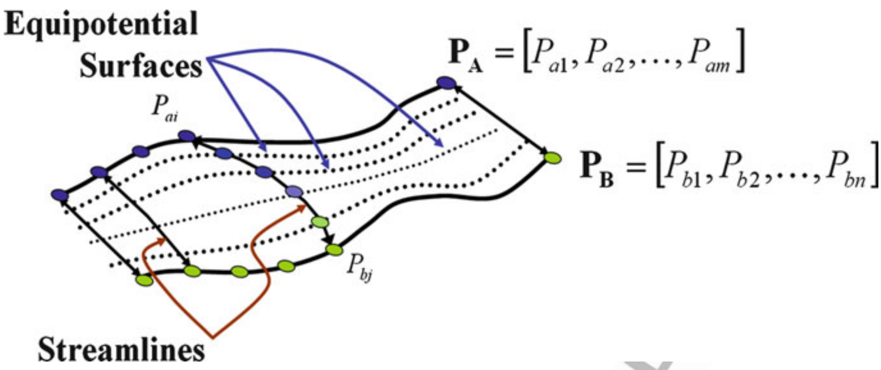

Fig. 9.10 Two dimensional illustration of the Laplace method

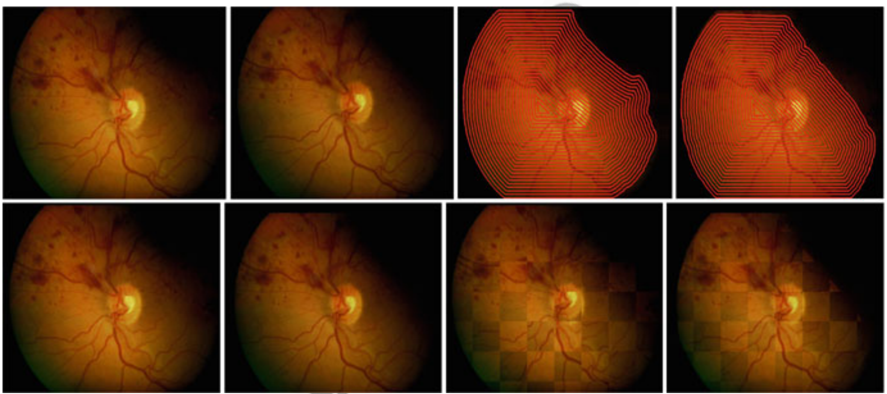

Fig. 9.11 Iso-contour-based retinal registration: from *left* to *right* in the *upper row* – the reference and target images and their respective iso-contours; in the *bottom row* – the reference and registered target images and the checkerboard visualization before and after the registration

models and analytical parameter estimates (e.g., contrast and offset in deriving the NCC). But these functions depend on the global or elastic geometric transformations $T_{\mathrm{g}}(\cdot)$ only implicitly, so that transformation parameters ensuring the best registration (i.e., the maximum similarity or minimum cost) have to be searched for by numerical techniques.

In the space of transformation parameters, the goal functions are usually multimodal, and the global optimum – the smallest cost or the largest similarity – with respect to all the possible solutions has to be found. Generally, global optimization means a full exhaustion of all the local optima that is feasible only in a parameter space of low cardinality (e.g., only translations). Today's global techniques constrain the exhaustion by adaptive parameter space exploration (e.g., to refine probabilities of candidate solutions) combined with local optimization. The latter explores a goal function only in a vicinity of each current location in the parameter space to successively move toward and eventually converge to the closest optimum.

The local techniques are sufficient and efficient for a continuous and well-behaved function with only one optimum [7] or, at least, when the search can be initiated closely to the global optimum. Medical image registration widely uses various local methods including the *Nelder–Mead downhill simplex method* [174], *Powell's direction set method* [175], the *Levenberg–Marquardt search* [176], *quasi-Newton* (variable metric) methods [177], and so forth. In many cases, these methods are efficient and result in sufficiently accurate registration in spite of their limited capture range and convergence to a local optimum in the parameter space. However, in general, no single best method exists for optimal image registration.

Multiresolution techniques (e.g., [178–181]) tend to increase the probability of finding the global optimum in the parameter space. The images are registered first at a low resolution, the optimal transformation found initiates the search at the next resolution level, and the process is repeated until the highest resolution level is reached. In practice, the multiresolution techniques were relatively robust to image noise, accelerated the optimization, and increased the capture range [181]. However, the search still is likely trapped in local optima because the global optimum may be absent at lower resolutions [1, 180]. More sophisticated techniques, including energy minimization, are used to accurately evaluate the transformation parameters [7]. A regularizing term can be added to the energy to penalize undesired geometric deviations of the target; see, e.g., [182, 183]. To make the global optimum more probable, complex stochastic optimization techniques, such as *genetic algorithms* (GA) [29], simulated annealing (SA) [30], particle swarm optimization (PSO) [31], evolutionary strategies (ES) [184], and the *tabu search* [185], are used sometimes.

Comprehensive comparisons of deterministic (e.g., steepest ascent or quasi-Newton) and stochastic (e.g., ES) gradient-based algorithms for nonrigid MI-based image registration with respect to speed, accuracy, and robustness can be found in [186]. Viola and Wells [6] found the maximum MI using the gradient ascent method. Thévenaz et al. [187] minimized the SSD cost function with the Levenberg–Marquardt method, while Wolberg and Zokai [188] applied the same registration to, respectively, deformed target images. Powell's multidimensional direction set method was used by Maes and Collignon [72]. The SA was applied in [189] to minimize the dissimilarity between the corresponding pairs of points, and the GA was used for image registration in [190]. Matsopoulos et al. [28] compared the accuracy and efficiency of the Nelder–Mead downhill simplex method, SA, and GA in registering retinal images under the affine and projective transformations.

9.2.4 Image Resampling

Geometric transformations assume a continuous image plane or volume. With respect to digital images on finite lattices, most of the transformations involve resampling, i.e. restoration of signals (e.g., gray levels) in locations mapped to the lattice points by transformation from the initial image signals [57]. From the theoretical viewpoint, only finite (band-limited) functions can be restored exactly from the lattice samples. However, natural images very rarely possess this property, so in practice only an approximate "continuous" image can be obtained by interpolating available discrete pixel- or voxel-wise signals.

Let $\mathbf{N}$ and $\mathbf{N}'$ denote an initial and destination image plane or volume, respectively, and let $T_g : \mathbf{N} \to \mathbf{N}'$ and $T_g^{-1} : \mathbf{N}' \to \mathbf{N}$ be a particular point-to-point geometric transformation (mapping) of $\mathbf{N}$ into $\mathbf{N}'$ and the inverse mapping. *Forward resampling* maps each pixel (voxel) $\mathbf{p}$ of the lattice in $\mathbf{N}$ to $\mathbf{N}'$ line with T_g and interpolates the mapped signals to find the pixel-wise (voxel-wise) signals for the lattice on $\mathbf{N}'$. As shown in Fig. 9.12, this method may leave holes and/or produce signal overlaps in the resampled images. *Backward resampling* escapes these drawbacks by using the inverse mapping and interpolating the signals on the initial plane (volume) $\mathbf{N}$.

Popular interpolation methods, such as the nearest neighbor, bilinear, bicubic spline, and radial symmetric kernel interpolation, vary in computational complexity and image restoration quality, the nearest neighbor and bilinear interpolation being the fastest. Most of these methods compute a weighted average of signals in the pixels (voxels) in an immediate neighborhood of the mapped location. Their detailed description is beyond the scope of this chapter. (A comprehensive analysis can be found in [191].)

Let, for simplicity, a 2-D image lattice have integer pixel coordinates, and let $\lfloor B \rfloor$ denote, as before, the integer part of a real-valued number B. The *nearest neighbor* interpolation assigns to a point (x, y) in the restored continuous image the gray value $I(l, m)$ of the closest pixel $\left(l = \lfloor x + 0.5 \rfloor,\ m = \lfloor y + 0.5 \rfloor\right)$. The *bilinear* interpolation combines the signals in up to four neighboring pixels.

$$I(x,y) = (1-s)(1-t)I(l,m) + s(1-t)I(l+1,m) + t(1-s)I_t(l,m+1) \\ + stI(l+1,m+1) \tag{9.22}$$

and the *bicubic* interpolation combines up to 4×4 neighbors:

$$I(x,y) = \sum_{i=-1}^{2} \sum_{j=-1}^{2} \beta^{[3]}(s-i)\beta^{[3]}(t-j)I(l+i,m+j) \tag{9.23}$$

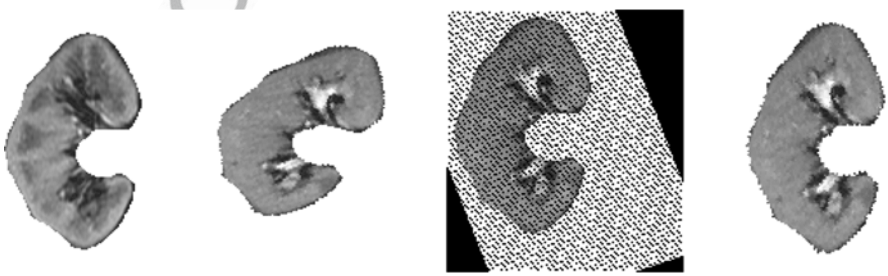

Fig. 9.12 Image resampling methods: from *left* to *right* – reference, target images, forward, and backward resampling for registration

where $l = \lfloor x \rfloor$, $m = \lfloor y \rfloor$, $s = x - l$ and $t = y - m$, and $\beta^{[3]}(u)$ is the basic cubic B-spline:

$$\beta^{[3]}(u) = \begin{cases} \frac{1}{6}(4 - 6|u|^2 + 3|u|^3) & \text{if } |u| \leqslant 1 \\ \frac{1}{6}(2 - |u|)^3 & \text{if } 1 < |u| \leqslant 2 \\ 0 & \text{if } |u| > 2 \end{cases} \tag{9.24}$$

The bicubic interpolation involves more computations (e.g., ≈10 times more than the nearest neighbor one). But it is more accurate than the two others and does not produce false boundaries as the nearest neighbor interpolation. Generally, the B-splines are very effective interpolants [192] having, in accord with Thévenaz et al. [191], the superior performance than any other polynomial basis function of the same order. The zero-order B-spline coincides with the nearest neighbor interpolant: $\beta^{[0]}(u) = 1$ if $|u| < 0.5$ and 0 otherwise. The n-order B-spline is obtained by convolving the $(n-1)$-order one with $\beta^{[0]}(u)$. In particular, the first-order B-spline is the linear interpolant: $\beta^{[1]}(u) = 1 - |u|$ if $|u| < 1$ and 0 otherwise.

The use of cubic splines in image interpolation was pioneered by Hou and Andrews [193]. In the limit $(n \to \infty)$, the B-spline converges to the Gaussian, and the corresponding interpolants rapidly converge to the sin c function $\sin \pi u / \pi u$ being optimal for exact restoration of finite functions [194]. However, even if the images were strictly bandlimited, the exact restoration is impossible because of the infinite support of the sin c function [191]. A truncated (usually called windowed) sin c function [195] uses a limited number of neighbors for interpolation but at the expense of larger restoration errors and artifacts [196].

The above resampling is not rotationally invariant. To obtain such invariance, one needs a radially symmetric interpolant combining a resampled value from the pixels within a circular area centered at the point of interest [197]. Popular examples of radially symmetric interpolants with elegant analytical properties are the Gaussians (e.g., [198]) and RBF (e.g., [199]).

9.3 Medical Image Registration for the Last Decade

Image registration in (9.1) is an (iterative) estimation of a parametric transformation ensuring the maximum similarity, or minimum cost, between the transformed target and reference images (Fig. 9.13). Roche et al. [200] considered the medical image registration as a maximum likelihood estimation problem to show that it fits to well-known similarity measures (e.g., NCC, correlation ratio, and MI) and used Powell's optimization method for rigid registration of 3-D brain images acquired for ten patients from different modalities (MR-T1, MR-T2, CT, and PET) and of an MR-T1-weighted scan to an intra-operative 3-D US image.

Likar and Pernus [201] proposed a hierarchical image subdivision strategy to perform an elastic registration of three differently stained serial transverse sections

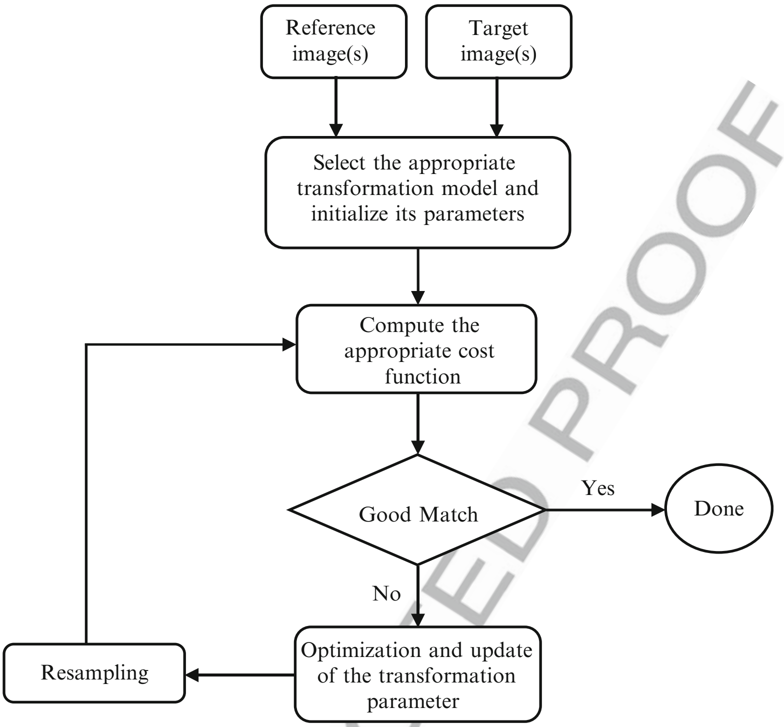

Fig. 9.13 Iterative image registration

of muscle fibers using the NMI. The nonrigid matching problem was decomposed into a TPS-based elastic interpolation of multiple local rigid registrations of sub-images of decreasing size. The marginal and joint intensity probability distributions were estimated by normalizing the joint intensity histogram.

Topology-preserving intersubject registration of medical images is of particular interest because no new structures appear, no existing structures disappear, and the connectedness of and neighborhood relationships between the structures are not affected. Musse et al. [202] proposed a parametric topology-preserving deformable image registration using a nonlinear Gauss–Seidel block algorithm to minimize the inter-image energy. Elegant linear constraints derived give the necessary and sufficient conditions for the determinant of the Jacobian of such transformations to be continuously positive everywhere. The method applies to the 2-D images only and is restricted to the first-order B-spline deformations.

A projection-based (or vector correlation) image registration algorithm proposed by Cain et al. [203] operates only on vectors as opposed to images. When compared with the classical NCC-based techniques, it was computationally efficient and accurate on images with a specific fixed-pattern noise of low SNR. However, only a global tip and tilt in an image can be removed, and the registered images retain all other distortions (e.g., caused by high-order atmospheric effects and laser speckles).

Kaneko et al. [204] proposed a parametric registration with an increment sign correlation (ISC) extending the NCC and coping with some occlusions, shadows, saturation, or illumination highlights of images or objects to be registered. But it fails if the occluding object has nonuniform brightness. A more robust modified ISC in [205], called selective correlation coefficient (SCC), filters the irrelevant pixels out by deriving a mask from the brightness increments.

Feature-based registration methods determine the transformation parameters from a set of control points extracted from each image. To improve the performance, recent studies (e.g., [206–208]) select the control points on the basis of local spatial frequencies of the signals. Liu et al. [206, 207] and Elbakary and Sundaresan [208] register multimodal medical images using banks of local Gabor and Gaussian filters to evaluate the frequencies. However, the number and characteristics of filters in the bank for given input images is to be selected ad hoc.

Extending the phase correlation to subpixel registration of multispectral images by analytic representation of down-sampling was pioneered by Foroosh et al. [36]. In spite of the analytic closed-form estimate of the subpixel translation, this method lacks the ability to evaluate mutual shifts greater than one pixel. Moreover, the phase-based similarity accounts for only translation, so more complex deviations may not be compensated appropriately.

Widely used in atlas-based segmentation, level set techniques have been tried for image registration, too (e.g., [209–211]). Vemuri et al. [209] and Bertalmio et al. [210] introduced a PDE-based joint registration and segmentation algorithm deduced from the general Osher–Sethian's level set evolution [212]. The higher dimensional level set function was replaced in [209] with the intensity function of an image to be registered (the target image), thus employing one PDE for registration. This algorithm has been tested on registering 3-D MRI. The registration of images from different modalities requires a different speed function. Two PDEs, one for morphing the image intensities as in [209] and the second for morphing the image contours, were used in [210]. Duay et al. [211] included more local prior information (e.g., the object's gray level distribution, shape, and contour curvature) in addition to the atlas. The main advantage is that any type of contours (closed, open, connected, or disconnected) can be registered. But the level set registration on the image intensities in [209, 210] can cause misregistration in the presence of local intensity differences between the images or a lesion in one of the images. The algorithm in [211] was tested only on 2-D synthetic and natural medical images.

An MI-based FFD registration of 3-D CT and PET chest images by Mattes et al. [13] uses continuous estimates of probability densities of signals with the Parzen windows [113] and a hierarchical multiresolution scheme to escape local minima and alleviate the need for accurate initialization. The goal function was split into two terms associated with the rigid and nonrigid deformations, respectively, to get both the criterion and its gradient in the closed form and use a quasi-Newton optimization technique. However, the authors pointed out that the results were unsatisfactory in the regions with larger deformations, such as at the diaphragm and abdomen. Also, only uniform image grids can be used, and this approach assumes a functional relation between the acquired transmission and emission PET images. A fully automated 3-D image registration by Zhu [111] uses cross-entropy (also called relative entropy or Kullback–Leibler distance) as a similarity measure and a multiresolution optimization. This approach had been tested on seven MR and nuclear transmission and emission brain images using the trilinear interpolation for volume resampling. However, it accounts for the rigid transformations only and is time consuming (computationally expensive).

Rohlfing et al. [182] used the NMI for nonrigid FFD registration of pre- and postcontrast breast MRI. Assuming the volume preserving local deformations, an incompressibility constraint – the unit determinant of the Jacobian of transformation – has been used. The goal function was penalized by adding the absolute log-Jacobian of the transformation or the squared second derivative for each voxel. The method was applied after making an initial affine transformation. An uphill-simplex algorithm restricted to the steepest ascent direction and a multiresolution optimization strategy were used to search for the optimum transformation parameters. But the flexibility of the method may be reduced due to the hard, regularizing incompressibility constraint. While the latter is well suited to intrasubject images, it may be unsuitable for intersubject image registration.

Noblet et al. [213] generalized the volume-preserving technique in [202] to 3-D B-spline deformations using a hierarchical first-order B-spline deformation field rather than the higher-order B-spline as in [13]. Unlike the above hard constraint [182], the determinant of the Jacobian is to be positive and within the two user-defined bounds in a continuous 3-D transformation domain. Due to difficulties of optimizing a 3-D B-spline-based deformable mapping, the maximum feasible step along the search direction that allows the determinant to remain in the feasible positive region is found by global optimization based on interval analysis [214]. This approach guarantees an invertible image-to-image transformation, but it is restricted to only linear B-splines because the higher-order splines result in the computationally too complex interval analysis.

D'Agostino et al. [19] proposed a multimodal MI-based FFD registration using a viscous fluid image model allowing for large local deformations, while maintaining a smooth one-to-one topology. The MI gradient with respect to individual voxel displacements is derived analytically from a differentiable, continuous joint probability density constructed with the Parzen window [113] from an empirical signal histogram. Experimental registration of simulated T1/T1, T1/T2, and T1/PD brain MRI showed good performance in both mono- and multimodal cases, but was very time consuming because a new PDE had to be solved iteratively at every step to find a vector field of velocities. Rohde et al. [78] refined the lattices using the gradient of global MI. Magnitudes of the gradient components were limited by bounding coefficients of the basis functions. An analytical sufficient condition to guarantee the positive Jacobian determinants was derived and achieved using a constrained optimization subject to a box constraint in the parameter space. This study focused only on 3-D brain images of non-articulated subjects (volumes with a small deformation range) that may be inadequate for articulated subjects with a considerably wider deformation range. Also, the search space is too restricted, e.g., large deformations with small gradients are not allowed.

Automatic analytical updates of steps for gradient descent optimization, cubic B-spline deformation models, and a multiresolution approach similar to [13, 111, 182, 215] were used in the SSD-based parametric elastic registration by Kybic and Unser [216]. External hints (landmarks) could be entered interactively to facilitate the correct solution. Efficiency of different local SSD-minimization algorithms (such as the gradient descent with feedback step adjustment or quadratic step estimation, the conjugated gradients, and the Levenberg–Marquardt algorithm) has been tested on simulated anatomical MRI.

Automatic 3-D-to-2-D-registration helps to transfer the acquired 3-D information to the 2-D data, to provide image-guided interventions, and to facilitate treatment planning. Penney et al. [217], Hipwell et al. [218], and Byrne et al. [219] developed automated intensity-based algorithms for updating a 3-D position of an interventional instrument using a single-plane angiogram registered to a 3-D volume. In particular, the algorithm by Penney et al. [217] for aligning preoperative CT and intraoperative fluoroscopy images was expanded to registering 3-D cerebral magnetic resonance angiography (MRA) with 2-D X-Ray angiograms [218] and matching 3-D X-ray digital subtraction angiography (3-D-DSA) images [219]. Comparative experiments in [217] gave surface-target registration errors of the order of 1–2 mm. Experimental selection of similarity measures for neurovascular interventions in [218] resulted in successful registrations of 95% of the phantom and 82% of the clinical images with the reprojection rms errors of 1.3 ± 0.6 and 1.5 ± 0.9 mm, respectively. The registration accuracy improves to 1.3 ± 0.6 mm in the clinical study for the two images of the same modality (3-D-DSA). Measuring the correspondence between the local intensity changes by the gradient difference in [218, 219] provides good registration results, but requires the contrast agent injection for the reference 2-D image. Furthermore, the computation time for these methods combined with the manual interaction to initiate the registration reduces possibilities of their wide integration into complete automatic toolkits [220]. The reader is referred to a comprehensive survey [221] of registering pre-interventional 3-D CT or MRI data to 2-D intra-interventional X-ray projection images.

The registration accuracy depends generally on the correctness of geometric transformation parameters. To improve the accuracy of their estimation, an improved FFD based on a hierarchical B-spline has been proposed in, e.g., [222–225]. A hierarchical B-spline contour-based registration by Xie and Farin [222] superposes FFD grids of different scales at various locations to provide a finer registration in certain areas. However, the global deformation still sums all the different-scale transformations. The algorithm is illustrated by both landmark- and intensity-based applications, but the validation is absent and the consistency of registration is not guaranteed. To analyze the heart local motion, Mora et al. [223] coupled the hierarchical B-spline with a variation-based level set. Tustison et al. [225] proposed a directly manipulated free-form deformation (DMFFD) model that improves the existing gradient-based FFD. The FFD- and DMFFD-based registration scenarios have been compared on both 2-D and 3-D images using different similarity or cost metrics (NCC, mean squares, and MI) and cubic B-splines. For a potentially faster image registration, the DMFFD framework calculates the gradient only in randomly selected points. It was shown that this framework overcomes problems of energy topography associated with the standard FFD. While the efficacy of the DMFFD was demonstrated for the random sampling-based registration, other nonuniform sampling strategies can improve the gradient approximations, too.

Proposed by Matsopoulos et al. [226] multimodal registration of retinal auto-fluorescence and infrared images uses a self-organizing map (SOM) to find the affine transformation minimizing differences between intensity gradients in specific pixels (landmarks) of the reference image and corresponding target points. Tests on the 24 pairs of multimodal images yielded the accuracy of approximately 40 μm for all the retinal pairs. However, the landmarks are difficult to extract in the case of hyperfluorescence, hemorrhages, or drusens, and the landmark correspondences are difficult to establish for small blood vessels at image periphery or in low-quality (blurred or noisy) images. An intensity-based registration by Kim and Fessler [227] uses a robust correlation coefficient to measure the similarity. It is less sensitive to outliers in one image, but not in the other, and was proven (both analytically and experimentally) to be more efficient than the MI-based registration.

Image registration can benefit from parallel implementations of its computationally intensive optimization algorithms. For example, the MI-based registration of multimodal images by Wachowiak and Peters [228] uses a coarse-grained parallel Powell's optimization. It is based on the global DIviding RECTangles (DIRECT) technique [229] and local multidirectional search (MDS) [230, 231] and increases the capture range for the goal optimum, but does not account for the memory locality. Lee et al. [232] presented a coordinate-invariant, geometric version of the Nelder–Mead optimization for the MI-based image registration. The computational efficiency on real 3-D CT and MRI increased by 15% compared with existing local coordinate-based methods. However, this approach may not be applicable for other similarity or cost measures and considers only the rigid-body transformation, while medical images have intrinsically nonrigid deformations.

Orchard [233] proposed an efficient globally exhaustive alignment search (GEAS) to perform the fast global optimization for multimodal image registration. The underlying SSD minimization was reformulated to be performed with the fast Fourier transform (FFT). The method was tested on aligning MR and CT head images, a chest CT image to a grayscale photo-image, antemortem to postmortem dental images, fingerprints, a grayscale photo to a gray-coded height map, and other images. However, the user's interaction is required to select an initial region-of-interest (ROI) for each image pair (with about 40% of the object in the overlapping portions of the images), and only a limited 2-D rigid-body transformation with the same scales and close orientations of the object is under consideration.

A SSD-based nonrigid registration by Sdika [234] uses nonlinear constraints to prevent spatial singularities or foldings due to zero or negative Jacobian determinants, respectively, of the transformation modeled with the cubic B-splines. To speed up the registration and avoid local minima in the high-dimensional parameter space, it uses a large-scale, constrained, nonlinear multiresolution optimization combining the method of multipliers and the low-memory Broyden–Fletcher–Goldfarb–Shanno algorithm (L-BFGS) with a monotone linear search. This approach ensures the local invertibility everywhere. However, calculating the Jacobian determinant or its gradient significantly increases the computation time due to additional B-spline interpolations of the partial derivatives of an image transformation. A framework for nonrigid image registration introduced by Glocker et al. [235] reformulates the registration problem in terms of Markov random field (MRF) models of images. Any similarity measure can be employed, and the optimization is tackled by quantizing the search space, thus making the problem completely discrete. But, the approach lacks the validation.

Recently, a number of rigid (e.g., [236, 237]) and nonrigid (e.g., [238–240]) registration algorithms have been applied to carotid images. The first MI-based 3-D rigid-body registration of MRA to *Power Doppler* US carotid images was proposed by Slomka et al. [236]. Fei et al. [237] introduced an automatic, NMI-based, rigid-body registration of multiple contrast-weighted MRI of carotid vessels that accounts for translations and rotations only (but not for scaling) and uses the uphill simplex optimization. But because different head positions during image acquisition cause relative bending and torsion in the neck, producing spatially variant image deformations, the transformation should be nonrigid. Chan et al. [238] proposed a nonrigid 3-D TPS-based registration of carotid MRI and 3-D US images that produced the mean registration error of approximately 1 mm on an ex vivo specimen. Krucker et al. [239] extended the TPS-based registration to synthetic and clinical breast images and tested the performance on 1.5–2.5 mm synthetic deformations and two phantom scans. Although the nonrigid registration in [238, 239] can capture mutual nonuniform image deformations due to different head positions, it is not always suitable for monitoring carotid plaque changes since it can alter existing plaque morphology during the registration. The computational cost is high due to the large number of registration parameters involved. Nanayakkara et al. [240] introduced an NMI-based nonrigid registration of 3-D US carotid images obtained at two different imaging sessions. Its "*twisting and bending*" model of nonuniform image deformations due to neck movements overcomes the plaque morphology alteration problem in [238, 239].

Sabuncu and Ramadge [241] introduced the first entropy-based algorithm for registering multimodal images that incorporates spatial information. Spatial feature vectors obtained from the images and a minimum spanning-tree approach are used to estimate the conditional higher-dimensional entropy: the Jensen-Renyi divergence between the learned and new joint intensity distributions is minimized with a gradient descent method. The method was compared with five different 3-D rigid registration algorithms on three simulated 3-D MRI sets of a healthy human brain and was shown to be fast. However, only simulated data and a rigid-body transformation were under consideration. Staring et al. [242] incorporated multiple image features, including the intensity gradients and Hessians (second derivative), into a nonrigid MI-based algorithm for registering cervical MRI. It employed a multiresolution and multifeatured approach combining the principal component analysis (PCA) to reduce the feature space, parametric cubic B-splines, and an iterative stochastic gradient ascent optimization [186, 243]. The reported median errors up to 3 mm with the third quartiles up to 5 mm for segmented clinical target volumes slightly outperformed results of the conventional MI-based registration.

Loeckx et al. [244] proposed a new intensity-based similarity measure, called the conditional mutual information (cMI), between the reference and target intensity distributions, given a certain spatial pixel distribution, and compared the cMI with the MI and *total correlation* introduced by Studholme et al. [245]. The algorithm uses analytical derivatives to avoid the discretization errors, a tensor-product B-spline image deformation model, and a limited memory quasi-Newton optimization. A parametric intensity-based registration framework by Bhagalia et al. [79] uses a multiresolution pyramid and an importance sampling (i.e., sampling of a subset of voxels on prominent image edges) to reduce the computational costs of calculating the MI gradient. Experiments on simulated brain MRI and real lung CT images from eight subjects showed that a combination of stochastic approximation-based optimization and importance sampling accelerates the registration while preserving the registration accuracy.

9.4 Conclusion

This chapter presented a brief review of medical image registration algorithms including the similarity or dissimilarity measures, rigid and elastic geometric transformations, popular numerical optimization methods, and image resampling. Image registration is considered as an optimal estimation of a geometric transformation that aligns partially overlapped target and reference images. The emphasis of the chapter is on describing most popular models and methods at each step of registration and pointing out their basic advantages and drawbacks. Some of the cutting-edge contributions to the medical image registration for the last decade are presented, too. But many important issues still remain to be solved, and the future research will likely focus on developing sophisticated, robust, efficient, and real-time approaches for nonrigid registration.

Appendix A: List of Symbols

I_{r}	Reference image.
I_{t}	Target image.
$T_{\mathrm{g}}(\cdot)$	Transformation function.
$\rho(\cdot)$	Cost function.
$\mathbf{p}$	Spatial coordinates vector.
$\tilde{\mathbf{p}}$	Homogeneous coordinates vector.

μ	Contrast deviation factor.
$\Gamma(\cdot)$	Random noise.
$\mathbf{W}$	Rectangular window or neighborhood system (regular and irregular).
$\bar{I}_{\mathrm{r}}$	Reference image mean value.
$\bar{I}_{\mathrm{t}}$	Target image mean value.
$F(.,.)$	2-D Fourier transform.
CPS_{F_1,F_2}	Normalized cross-power spectrum.
$\mathbf{X}$ and $\mathbf{Y}$	Finite signal sets.
ϕ and ψ	One-to-one mappings.
p_i and q_j	Marginal probability distributions.
p_{ij}	Joint probability distribution of two random variables.
$p_{i\|j}$	Conditional probability distribution.
$H(\cdot)$	Shannon Entropy.
$H(\cdot\|\cdot)$	Conditional Entropy.
$H(\cdot,\cdot)$	Joint Entropy.
$\Delta = (\delta_x, \delta_y, \delta_z)$	Spatial offsets vector.
$E(\cdot)$	Gibbs energy.
$\mathbf{V}_\Delta$	Potential function.
$\mathbf{F}_\Delta$	Empirical probability of signal co-occurrences in the MGRF clique Family.
λ	Relative cardinality of the MGRF model.
τ	Arbitrary scale factor.
θ	Angel in radians.
$\boldsymbol{\alpha} = (\alpha_x, \alpha_y, \alpha_z)$	Scaling vector.
ζ_x and ζ_y	$x$and y-Shearing Factors.
$\mathbf{a} = (a_{11}, a_{12}, a_{13}, a_{14}, \ldots, a_{33}, a_{34})$, $\mathbf{b} = (b_{11}, b_{12}, b_{13}, \ldots, b_{23})$, and $\mathbf{c} = (c_{11}, c_{12}, c_{21}, c_{22})$	Rigid transformation coefficients vectors.
$\mathbf{A} = (a_{00}, a_{10}, a_{01}, a_{02}, a_{20}, a_{03}, a_{000}, a_{100}, a_{010}, a_{001})$, $\mathbf{B} = (b_{00}, b_{10}, b_{01}, b_{02}, b_{20}, b_{03})$	Global polynomial and spline numerical coefficients.
F_k	Spline distance weight coefficients.
η^2	Spline stiffness coefficient.
r	Cartesian distance between two points.
Φ	Control points lattice (mesh).
γ	Lattice (mesh) spacing.
N	Number of control points.
$\beta = (\beta_{-1}, \beta_0, \beta_1, \beta_2)$	uniform cubic B-spline basis functions.

$R_k(.,.)$	Radial basis function.
σ	Standard deviation.
$\mathbf{N},\mathbf{N}'$	Reference and target image planes (volumes).
$\beta^{[n]}(\cdot)$	n-order B-spline.

References

1. Hill DLG, Batchelor PG, Holden M, Hawkes DJ (2001) Medical image registration. Phys Med Biol 46(3):R1–R45
2. Hallpike L, Hawkes DJ (2002) Medical image registration: an overview. Imaging (Br Inst Radiol) 14(6):455–463
3. Khaissidi G, Tairi H, Aarab A (2009) A fast medical image registration using feature points. Int J Graph Vis Image Process (GVIP) 9(3)
4. Li H, Manjunath BS, Mitra SK (1995) A contour-based approach to multisensor image registration. IEEE Trans Image Process 4(3):320–334
5. Xia M, Liu B (2004) Image registration by super-curves. IEEE Trans Image Process 13 (4):720–732
6. Viola P, Wells WM III (1997) Alignment by maximization of mutual information. Int J Comput Vis 24(2):137–154
7. Collignon A, Maes F, Delaere D, Vandermeulen D, Suetens P, Marchal G (1995) Automated multimodality medical image registration using information theory. In: Proceeding of the 14th international conference on information processing in medical imaging (IPMI'95), June 1995, pp 263–274
8. Azar A, Xu C, Pennec X, Ayache N (2006) An interactive hybrid non-rigid registration framework for 3-D medical images. In: Proceeding of the international symposium on biomedical imaging (ISBI'06), Arlington, Virginia, April, pp 824–827
9. Cachier P, Mangin J-F, Pennec X, Rivière D, Orfanos DP, Régis J, Ayache N (2001) Multisubject non-rigid registration of brain MRI using intensity and geometric features. In: Proceeding of the 4th international conference on medical image computing and computer-assisted intervention (MICCAI'01), October 2001, pp 734–742
10. Hellier P, Barillot C (2003) Coupling dense and landmark-based approaches for nonrigid registration. IEEE Trans Med Imaging 22(2):217–227
11. West J, Fitzpatrick JM, Wang MY et al (1997) Comparison and evaluation of retrospective intermodality brain image registration techniques. J Comput Assist Tomogr 21(4):554–566
12. Hurvitz A, Joskowicz L (2008) Registration of a CT-like atlas to fluoroscopic X-ray images using intensity correspondences. Int J Comput Assist Radiol Surg 3(6):493–504
13. Mattes D, Haynor DR, Vesselle H, Lewellen TK, Eubank W (2003) PET-CT image registration in the chest using free-form deformations. IEEE Trans Med Imaging 22(1):120–128
14. Rueckert D, Sonoda LI, Hayes C, Hill DL, Leach MO, Hawkes DJ (1999) Nonrigid registration using free-form deformations: application to breast MR images. IEEE Trans Med Imaging 18(8):712–721
15. Bookstein FL (1989) Principal warps: thin-plate splines and the decomposition of deformations. IEEE Trans Pattern Anal Mach Intell 11(6):567–585
16. Bajcsy R, Kovacic S (1989) Multiresolution elastic matching. Comput Vis Graph Image Process 46(1):1–21
17. Davis MH, Khotanzad A, Flamig DP, Harms SE (1997) A physics-based coordinate transformation for 3-D image matching. IEEE Trans Med Imaging 26(3):317–328
18. Gee JC (1999) On matching brain volumes. Pattern Recognit 32(1):99–111

19. D'Agostino E, Maes F, Vandermeulen D, Suetens P (2003) A viscous fluid model for multimodal non-rigid image registration using mutual information. Med Image Anal 7(4):565–575
20. Avants B, Gee JC (2004) Geodesic estimation for large deformation anatomical shape averaging and interpolation. Neuroimage 23(1):S139–S150
21. Fischer B, Modersitzki J (2004) A unified approach to fast image registration and a new curvature based registration technique. Linear Algebra Appl 380:107–124
22. Arsigny V, Pennec X, Ayache N (2005) Polyrigid and polyaffine transformations: A novel geometrical tool to deal with non-rigid deformations application to the registration of histological slices. Med Image Anal 9(6):507–523
23. du Bois d'Aische A, Craene MD, Geets X (2005) Efficient multimodal dense field nonrigid registration: alignment of histological and section images. Med Image Anal 9(6):538–546
24. Beg F, Miller M, Trouve A, Younes L (2005) Computing large deformation metric mappings via geodesic flows of diffeomorphisms. Int J Comput Vis 61(2):139–157
25. Vercauteren T, Pennec X, Perchant A, Ayache N (2009) Diffeomorphic demons: efficient non-parametric image registration. Neuroimage 45(1):S61–S72
26. Jacoby SLS, Kowalik JS, Pizzo JT (1972) Iterative methods for nonlinear optimization problems. Prentice Hall, Englewood Cliffs, NJ
27. Press W, Flannery B, Teukolsky S, Vetterling W (1992) Numerical recipes in C. Cambridge University Press, Cambridge, UK
28. Matsopoulos GK, Mouravliansky NA, Delibasis KK, Nikita KS (1999) Automatic retinal image registration scheme using global optimization techniques. IEEE Trans Info Technol Biomed 3(1):47–60
29. Goldberg D (1989) Genetic algorithms in optimization, search and machine learning. Addison-Wesley, Reading, MA
30. Aarts E, Laardhoven Van (1987) Simulated annealing: theory and practice. Wiley, New York
31. Kennedy J, Eberhart R (1995) Particle swarm optimization. In: Proceeding of the IEEE international conference neural network, Perth, Australia, November 1995, vol 4, pp 1942–1945
32. Wolberg G, Zokai S (2000) Robust image registration using log-polar transform. In: Proceeding of the IEEE international conference image process (ICIP'00), Vancouver, BC, Canada, September 2000, vol 1. pp 493–496
33. Kuglin CD, Hines DC (1975) The phase correlation image alignment method. In: Proceeding of the IEEE International Conference Cybern Society, September 1975, pp 163–165
34. Reddy S, Chatterji BN (1996) An FFT-based technique for translation, rotation, and scale invariant image registration. IEEE Trans Image Process 3(8):1266–1270
35. Milanfar P (1996) Projection-based, frequency-domain estimation of superimposed translational motions. J Opt Soc Am A Opt Image Sci 13(11):2151–2162
36. Foroosh H, Zerubia J, Berthod M (2002) Extension of phase correlation to subpixel registration. IEEE Trans Image Process 11(3):188–200
37. Chen Q, Defrise M, Deconinck F (1994) Symmetric phase-only matched filtering of Fourier-Mellin transforms for image registration and recognition. IEEE Trans Pattern Anal Mach Intell 16(12):1156–1168
38. De Castro E, Morandi C (1987) Registration of translated and rotated images using finite Fourier transforms. IEEE Trans Pattern Anal Mach Intell 9(5):700–703
39. Casasent D, Psaltis D (1976) Position, rotation, and scale invariant optical correlation. Appl Opt 15:1793–1799
40. Lehmann TM (1998) A two stage algorithm for model-based registration of medical images. In: Proceeding of the international conference on pattern recognition. (ICPR'98), Brisbane, Australia, August 1998, vol 1. pp 344–352
41. Lehmann T, Goerke C, Schmitt W, Kaupp A, Repges R (1996) A rotation-extended cepstrum technique optimized by systematic analysis of various sets of X-ray image. Proc SPIE Med Imaging Image Process 2710:390–401

42. Wang J, Reinstein LE, Hanley J, Meek AG (1996) Investigation of a phase-only correlation technique for anatomical alignment of portal images in radiation therapy. Phys Med Biol 41 (6):1045–1058
43. Shekarforoush H, Berthod M, Zerubia J (1996) Subpixel image registration by estimating the polyphase decomposition of cross power spectrum. In: Proceeding of the IEEE computer society conference on computer vision and pattern recognition (CVPR'96), Los Alamitos, CA, June 1996, pp 532–537
44. Zokai S, Wolberg G (2005) Image registration using log-polar mappings for recovery of large scale similarity and projective transformations. IEEE Trans Image Process 14(10):1422–1434
45. Matungka R, Zheng YF, Ewing RL (2009) Image registration using adaptive polar transform. IEEE Trans Image Process 18(10):2340–2354
46. Wang X, Feng DD (2009) Non-iterative hierarchical registration for medical images. J Signal Process Sys 54(1–3):65–77
47. Arora H, Namboodiri AM, Jawahar CV (2008) Robust image registration with illumination, blur, and noise variation for super-resolution. In: Proceeding of the IEEE international conference on acoustics, speech, and signal processing (ICASSP'08), Las Vegas, NV, March 2008, pp 1301–1304
48. Vandewalle P, Süsstrunk S, Vetterli M (2006) A frequency domain approach to registration of aliased images with application to super-resolution. J Appl Signal Process 2006:1–14 (article ID 71459)
49. van Dalen JA, Huisman HJ, Welmers A, Barentsz JO (2003) Semi-automatic image registration of MRI to CT data of the prostate using gold markers as fiducials. In: 2nd International workshop on biomedical image registration (WBIR'03), Revised Papers (Lecture notes in computer science), vol 2717. Philadelphia, PA, 23–24 June 2003, pp 311–320
50. Qiao F, Yue Y, Pan T, Clark JW Jr, Mawlawi O (2004) Segmentation of contrast enhanced CT images for attenuation correction of PET/CT data. In: Nuclear science symposium conference record, Rome, Italy, October 2004, vol 5. pp 2686–2689
51. Woods RP, Mazziotta JC, Cherry SR (1993) MRI-PET registration with automated algorithm. J Comput Assist Tomogr 17(4):536–546
52. Gill S, Mousavi P, Fichtinger G, Pichora D, Abolmaesumi P (2009) Group-wise registration of ultrasound to CT images of human vertebrae. In: Proceeding of the SPIE medical imaging: visualization, image-guided procedures, and modeling, vol 7261, pt 1, pp 72611O-1–72611O-9
53. Periaswamy S, Farid H (2006) Medical image registration with partial data. Med Image Anal 10(3):452–464
54. Brown L (1992) A survey of image registration techniques. ACM Comput Surv 24(4):326–376
55. Maurer CR, Fitzpatrick T (1993) A review of medical image registration. Interact Image Guided Neurosurg 17–44
56. van den Elsen PA, Pol E-J, Viergever MA (1993) Medical image matching: a review with classification. IEEE Eng Med Biol 12:26–39
57. Maintz JBA, Viergever MA (1998) A survey of medical image registration. Med Image Anal 2(1):1–36
58. Lester H, Arridge SR (1999) A survey of hierarchical non-linear medical image registration. Pattern Recognit 32:129–149
59. Zitova B, Flusser J (2003) Image registration methods: a survey. Image Vis Comput 21(11):977–1000
60. Amit Y (1997) Graphical shape templates for automatic anatomy detection with applications to MRI brain scan. IEEE Trans Med Imaging 16(1):28–40
61. Subsol G, Thirion JP, Ayache N (1998) A general scheme for automatically building 3-D morphometric anatomical atlases: application to a skull atlas. Med Image Anal 2(1):37–60

62. Ge Y, Fitzpatrick JM, Kessler RM, Janicka MJ (1995) Inter-subject brain image registration using both cortical and subcortical landmarks. Proc SPIE Med Imaging Image Process 2434:81–95
63. Can A, Stewart CV, Roysam B, Tanenbaum HL (2002) A feature-based, robust, hierarchical algorithm for registering pairs of images of the curved human retina. IEEE Trans Pattern Anal Mach Intell 24(3):347–364
64. Szeliski R, Lavallee S (1994) Matching 3-D anatomical surfaces with nonrigid deformations using octree-splines. In: Proceedings of the IEEE workshop on biomedical image analysis, Seattle, WA, June 1994, pp 144–153
65. Thompson PM, Toga AW (1996) A surface-based technique for warping 3-dimensional images of the brain. IEEE Trans Med Imaging 15(4):402–417
66. Audette MA, Ferrie FP, Peters TM (2000) An algorithmic overview of surface registration techniques for medical imaging. Med Image Anal 4(3):201–217
67. Lowe DG (2004) Distinctive image features from scale-invariant keypoints. Int J Comput Vis 60(2):91–110
68. Yasein MS, Agathoklis P (2008) A feature-based image registration technique for images of different scale. In: Proceedings of the IEEE international symposium on circuits and systems (ISCAS'08), Seattle, WA, May 2008, pp 3558–3561
69. Pope P, Theiler J (2003) Automated image registration (AIR) of MTI imagery. Proc SPIE 27:294–305
70. Barnea DI, Silverman HF (1972) A class of algorithms for fast digital image registration. IEEE Trans Comput C-21(2):179–186
71. Althof RJ, Wind MG, Dobbins JT (1997) A rapid and automatic image registration algorithm with subpixel accuracy. IEEE Trans Med Imaging 16(3):308–316
72. Maes F, Collignon A (1997) Multimodality image registration by maximization of mutual information. IEEE Trans Med Imaging 16(2):187–198
73. Chen H-M, Varshney PK (2000) A pyramid approach for multimodality image registration based on mutual information. In: Proceedings of the 3rd international conference on information fusion (ISIF'00), July 2000, I:9–I:15
74. Pluim JPW, Maintz JBA, Viergever MA (2000) Image registration by maximization of combined mutual information and gradient information. IEEE Trans Med Imaging 19(8):809–814
75. Netsch T, Rosch P, Muiswinkel A, Weese J (2001) Towards real-time multi-modality 3-D medical image registration. In: Proceeding of the 8th international conference on computer vision (ICCV'01), Vancouver, BC, Canada, July 2001, vol 1, pp 718–725
76. Shekhar R, Zagrodsky V (2002) Mutual information-based rigid and nonrigid registration of ultrasound volumes. IEEE Trans Med Imaging 21(1):9–22
77. Tsao J (2003) Interpolation artifacts in multimodality image registration based on maximization of mutual information. IEEE Trans Med Imaging 22(7):854–863
78. Rohde GK, Aldroubi A, Dawant BM (2003) The adaptive bases algorithm for intensity based nonrigid image registration. IEEE Trans Med Imaging 22(11):1470–1479
79. Bhagalia R, Fessler JA, Kim B (2009) Accelerated nonrigid intensity-based image registration using importance sampling. IEEE Trans Med Imaging 28(8):1208–1216
80. Peng X, Ding M, Zhou C, Ma Q (2004) A practical two-step image registration method for two-dimensional images. Inf Fusion 5(4):283–298
81. Hipwell J, Tanner C, Crum W, Hawkes D (2006) X-ray mammogram registration: a novel validation method. In: Proceeding of the 8th international workshop on digital mammography (IWDM'06), Manchester, UK, 18–21 June 2006 (Lecture notes in computer science), vol 4046. pp 197–204
82. Studholme C, Hill DLG, Hawkes DJ (1999) An overlap invariant entropy measure of 3-D medical image alignment. Pattern Recognit 32(1):71–86
83. Bracewell RN (1965) The Fourier transform and its applications. McGraw-Hill, New York
84. Junck L, Moen JG, Hutchins GD, Brown MB, Kuhl DE (1990) Correlation methods for the centering, rotation, and alignment of functional brain images. J Nucl Med 31(7):1220–1276

85. van den Elsen PA, Viergever MA (1993) Automated CT and MR brain image registration using geometrical feature correlation. In: Proceedings of the nuclear science symposium and medical imaging conference, San Francisco, CA, November 1993, vol 3. pp 1827–1830
86. van den Elsen PA, Pol EJ, Sumanaweera TS, Hemler PF, Napel S, Adler J (1994) Grey value correlation techniques used for automatic matching of CT and MR brain and spine images. Proc SPIE Vis Biomed Comput 2359:227–237
87. Radcliffe T, Rajapakshe R, Shalev S (1994) Pseudocorrelation: a fast, robust, absolute, grey level image alignment algorithm. Med Phys 21(6):761–769
88. McParland BJ, Kumaradas JC (1995) Digital portal image registration by sequential anatomical matchpoint and image correlations for real-time continuous field alignment verification. Med Phys 22(7):1063–1075
89. Andersson JLR (1995) A rapid and accurate method to realign PET scans utilizing image edge information. J Nucl Med 36(4):657–669
90. Dong L, Boyer AL (1996) A Portal image alignment and patient setup verification procedure using moments and correlation techniques. Phys Med Biol 41(4):697–723
91. Goshtasby A, Gage SH, Bartholic JF (1984) A two-stage cross-correlation approach to template matching. IEEE Trans Pattern Anal Mach Intell 6(3):374–378
92. Lewis JP (1995) Fast template matching. In: Proceedings of the Canadian image processing pattern recognition society conference on vision interface, Quebec City, Canada, May 1995, pp 120–123
93. Berthilsson R (1998) Affine correlation. In: Proceedings of the 14th international conference on pattern recognition (ICPR'98), Brisbane, Australia, August 1998, vol 2. pp 1458–1461
94. Zhao F, Huang Q, Gao W (2006) Image matching by normalized cross-correlation. In: Proceeding of the IEEE international conference on acoustics, speech, and signal processing, Toulouse, May 2006, vol 2. pp 729–732
95. Yeung MM, Yeo B, Liou S, Hashemi AB (1994) Three-dimensional image registration for spiral CT angiography. In: Proceeding of the IEEE computer society conference on computer vision and pattern recognition (CVPR'94), Los Alamitos, CA, June 1994, pp 423–429
96. Christensen GE, Rabbitt RD, Miller MI, Joshi SC, Grenander U, Coogan TA, Van Essen DC (1995) Topological properties of smooth anatomic maps. In: Proceedings of the 16th international conference on information processing medical imaging (IPMI'95), Ile de Berder, France, June 1995, pp 101–112
97. Hajnal JV, Saeed N, Oatridge A, Williams EJ, Young IR, Bydder GM (1995) Detection of subtle brain changes using subvoxel registration and subtraction of serial MR images. J Comput Assist Tomogr 19(5):677–691
98. Guimond A, Roche A, Ayache N, Meunier J (2001) Three-dimensional multimodal brain warping using the demons algorithm and adaptive intensity corrections. IEEE Trans Med Imaging 20(1):58–69
99. Periaswamy S, Farid H (2003) Elastic registration in the presence of intensity variations. IEEE Trans Med Imaging 22(7):865–874
100. Unser M, Thevenaz P, Lee C, Ruttimann UE (1995) Registration and statistical analysis of PET images using the wavelet transform. IEEE Eng Med Biol 14(5):603–611
101. Eberl S, Kanno I, Fulton RR, Ryan A, Hutton BF, Fulham MJ (1996) Automated interstudy image registration technique for SPECT and PET. J Nucl Med 37(1):137–145
102. Haller JW, Christensen GE, Joshi SC, Newcomer JW, Miller MI, Csernansky JG, Vannier MW (1996) Hippocampal MR imaging morphometry by means of general pattern matching. Radiology 199(3):787–791
103. Bhat DN, Nayar SK (1998) Ordinal measures for image correspondence. IEEE Trans Pattern Anal Mach Intell 20(4):415–423
104. Studholme C (1997) Measures of 3-D medical image alignment. Ph.D. thesis, University of London, London, UK
105. Viola PA (1995) Alignment by maximization of mutual information. Ph.D. thesis, Massachusetts Institute of Technology, Artificial Intelligence Laboratory

106. Wells WM III, Viola P, Atsumi H, Nakajima S, Kikinis R (1996) Multi-modal volume registration by maximization of mutual information. Med Image Anal 1(1):35–51
107. Maes F, Vandermeulen D, Suetuns P (2003) Medical image registration using mutual information. IEEE Proc 91(10):1699–1722
108. Collignon A, Vandermeulen D, Suetens P, Marchal G (1995) 3D multi-modality medical image registration using feature space clustering. In: Proceedings of the 1st international conference on computer vision, virtual reality and robotics in medicine, Nice, France, April 1995, pp 195–204
109. Studholme C, Hill D, Hawkes D (1995) Multiresolution voxel similarity measures for MR-PET registration. In: Bizais Y, Barillot C, di Paola R (eds) Information processing in medical imaging. Kluwer Academic Publishers, Dordrecht, The Netherlands, pp 287–298
110. Rangarajan A, Chui H, Duncan JS (1999) Rigid point feature registration using mutual information. Med Image Anal 3(4):1–17
111. Zhu YM (2002) Volume image registration by cross-entropy optimization. IEEE Trans Med Imaging 21(2):174–180
112. Pluim JPW, Maintz JBA, Viergever MA (2004) f-information measures in medical image registration. IEEE Trans Med Imaging 23(12):1508–1516
113. Parzen E (1962) On the estimation of probability density function. Ann Math Stat 33:1065–1076
114. Niu C (2005) Medical image registration based on mutual information using Kriging probability density estimation. In: Proceedings of the IEEE 27th annual conference engineering in medicine and biology, Shanghai, China, September 2005, pp 3097–3099
115. Rangarajan A, Duncan JS (1998) Matching point features using mutual information. In: Proceedings of the IEEE workshop on biomedical image analysis (WBIA'98), Santa Barbara, CA, June 1998, pp 172–181
116. Liu C, Li K, Liu Z (2005) Medical image registration by maximization of combined mutual information and edge correlative deviation. In: Proceeding of the IEEE 27th annual conference engineering in medicine and biology, Shanghai, China, September 2005, pp 6379–6382
117. El-Baz A, Gimel'farb G (2007) A new framework for automatic registration of 2D/3D texture images. In: Proceedings of the British machine vision conference (BMVC'07), University of Warwick, UK, September 2007, pp 100–109
118. El-Baz A, Gimel'farb G (2008) Global image registration based on learning the prior appearance model. In: Proceeding of IEEE conference on computer vision pattern recognition (CVPR'08), Anchorage, AK, June 2008, pp 1–7
119. Woods RP, Cherry SR, Mazziotta JC (1992) Rapid automated algorithm for aligning and reslicing PET images. J Comput Assist Tomogr 16(4):620–633
120. Freeborough PA, Fox NC (1997) The boundary shift integral: an accurate and robust measure of cerebral volume changes from registered repeat MRI. IEEE Trans Med Imaging 16(5):623–629
121. Hill DLG (1993) Combination of 3-D medical images from multiple modalities. Ph.D. thesis, University of London
122. Hill DL, Hawkes DJ, Harrison NA, Ruff CF (1993) A strategy for automated multimodality image registration incorporating anatomical knowledge and imager characteristics. In: Proceedings of the 13th international conference on information processing in medical imaging (IPMI'93), June 1993, pp 182–196
123. Ardekani BA, Braun M, Kanno I, Hutton BF (1994) Automatic detection of intradural spaces in MR images. J Comput Assist Tomogr 18(6):963–969
124. Zuo CS, Jiang A, Buff BL, Mahon TG, Wong TZ (1996) Automatic motion correction for breast MR imaging. Radiology 198(3):903–906
125. Cox GS, de Jager G (1994) Automatic registration of temporal image pairs for digital subtraction angiography. Proc SPIE Med Imaging Image Process 2167:188–199
126. Ardekani BA, Braun M, Hutton BF, Kanno I, Lida H (1995) A fully automatic multimodality image registration algorithm. J Comput Assist Tomogr 19(4):615–623

127. Buzug T, Weese J (1996) Improving DSA images with an automatic algorithm based on template matching and an entropy measure. Comput Assist Radiol 1124:145–150
128. Hill DLG, Studholme C, Hawkes DJ (1994) Voxel similarity measures for automated image registration. Proc SPIE Vis Biomed Comput 2359:205–216
129. Venot A, Golmard JL, Lebruchec JF, Pronzato L, Walter E, Frij G, Roucayrol JC (1983) Digital methods for change detection in medical images. In: Proceedings of the 9th conference on information processing in medical imaging (IPMI'83), June 1983, vol 8, pp 1–16
130. Venot A, Lebruchec JF, Roucayrol JC (1984) A new class of similarity measures for robust image registration. Comput Vis Graph Image Process 28(3):176–184
131. Venot A, Leclerc V (1984) Automated correction of patient motion and gray values to subtraction in digitized angiography. IEEE Trans Med Imaging 3(4):179–186
132. Hua P, Fram I (1993) Feature-based image registration for digital subtraction angiography. Proc SPIE Med Imaging Image Process 1898:24–31
133. Hoh CK, Dahlbom M, Harris G, Choi Y, Hawkins RA, Phelps ME, Maddahi J (1993) Automated iterative three-dimensional registration of positron emission tomography images. J Nucl Med 34(11):2009–2018
134. Venot A, Pronzato L, Walter E (1994) Comments about the coincident bit counting (CBC) criterion for image registration. IEEE Trans Med Imaging 13(3):565–566
135. Perault C, Wampach H, Liehn J, Three dimensional SPECT myocardial rest-stress subtraction images after automated registration and normalization. In: Bizais Y et al. (eds) Proceeding of the 14th international conference on information processing medical images (IPMI'95), Kluwer Academic, Dordrecht, The Netherlands, pp 391–392
136. Hashemi AB, Krishnan A, Samaddar S (1996) Warped matching for digital subtraction of CT-angiography studies. Proc SPIE Med Imaging Image Process 2710:428–437
137. Shields K, Barber DC, Sheriff SB (1993) Image registration for the investigation of atherosclerotic plaque movement. In: Proceedings of the 13th international conference on information processing in medical imaging (IPMI'93), June 1993, vol 687, pp 438–458
138. Bandari E, Xiang QS, Little J (1994) Visual echo registration of magnetic resonance images. In: Application of computer vision medical image processing (AAAI'94), Spring Symposium Series, Stanford University, Stanford, CA, pp 38–41
139. Barber DC, Tindale WB, Hunt E, Mayes A, Sagar HJ (1995) Automatic registration of SPECT images as an alternative to immobilization in neuroactivation studies. Phys Med Biol 40(3):449–463
140. Meunier J, Guimond A, Janicki C, Imbert B, Soucy J (1996) Automatic 3-D registration of brain SPECT images. In: Proceeding of the international congress of computational assisted radiology (Excerpta Medica– international congress series), vol 1124, pp 187–192
141. Little JA, Hill DLG, Hawkes DJ (1997) Deformations incorporating rigid structures. Comput Vis Image Understand 66(2):223–232
142. Zagorchev L, Goshtasby A (2006) A comparative study of transformation functions for nonrigid image registration. IEEE Trans Image Process 15(3):529–538
143. Rivlin TJ (1969) Least-squares approximation. In: An introduction to the approximation of functions, Blaisdell Publishing Company, New York, pp 48–65
144. Stockman G, Kopstein S, Benett S (1982) Matching images to models for registration and object detection via clustering. IEEE Trans Pattern Anal Mach Intell 4(3):229–241
145. Harder RL, Desmarais RN (1972) Interpolation using surface splines. J Aircraft 9(2):189–191
146. Meinguet J (1978) An intrinsic approach to multivariate spline interpolation at arbitrary points, polynomial and spline approximation. In: Proceedings of the NATO advanced study institute, Calgary, Canada, August, pp 163–190
147. Goshtasby A (1988) Registration of image with geometric distortion. IEEE Trans Geosci Remote Sens 26(1):60–64
148. Grimson WEL (1982) A computational theory of visual surface interpolation. Philos Trans R Soc Lond B Biol Sci 298(1092):395–427

149. Chui H, Rangarajan A (2000) A new algorithm for non-rigid point matching. In: Proceedings of the IEEE conference on computer vision and pattern recognition (CVPR'00), Hilton Head Island, SC, June 2000, vol 2. pp 44–51
150. Johnson HJ, Christensen GE (2002) Consistent landmark and intensity-based image registration. IEEE Trans Med Imaging 21(5):450–461
151. J Lim, MH Yang. A direct method for modeling non-rigid motion with thin plate spline. In: Proceedings of the IEEE conference on computer vision and pattern recognition (CVPR'05), July 2005, vol 1. pp 1196–1202
152. Eriksson AP, Astrom K (2006) Bijective image registration using thin-plate splines. In: Proceedings of the 18th IEEE international conference on pattern recognition (ICPR'06), Hong Kong, China, September 2006, vol 3. pp 798–801
153. Greengard L, Rokhlin V (1987) A fast algorithm for particle simulations. J Comput Phys 73 (2):325–348
154. Beatson RK, Newsam GN (1992) Fast evaluation of radial basis functions. Int J Comput Math Appl 24(12):7–19
155. Flusser J (1992) An adaptive method for image registration. Pattern Recognit 25(1):45–54
156. Barrodale I, Skea D, Berkley M, Kuwahara R, Poeckert R (1993) Warping digital images using thin plate splines. Pattern Recognit 26(2):375–376
157. Rohr K (2001) Landmark-based image analysis using geometric and intensity models (computational imaging and vis. series). Kluwer Academic, Dordrecht, The Netherlands
158. Evans AC, Dai W, Collins L, Neelin P, Marrett S (1991) Warping of a computerized 3-D atlas to match brain image volumes for quantitative neuroanatomical and functional analysis. Proc SPIE Med Imaging Image Process 1445:236–247
159. Sederberg TW, Parry SR (1986) Free-form deformation of solid geometric models. Comput Graph 20(4):151–160
160. Lee S, Wolberg G, Chwa K-Y, Shin SY (1996) Image metamorphosis with scattered feature constraints. IEEE Trans Vis Comput Graph 2(4):337–354
161. Lee S, Wolberg G, Shin SY (1997) Scattered data interpolation with multilevel B-splines. IEEE Trans Vis Comput Graph 3(3):228–244
162. Arad N, Dyn N, Reisfeld D, Yeshurun Y (1994) Image warping by radial basis functions: application to facial expressions. Graph Models Image Process 56(2):161–172
163. Arad N, Reisfeld D (1995) Image warping using few anchor points and radial functions. Comput Graph Forum 14, no.1:35–46
164. Ruprecht D, Muller H (1993) Free form deformation with scattered data interpolation methods. In: Hagen H, Noltemeier H, Farin G (eds) Geometric modelling (computing supplementum 8). Springer Verlag, Wien, Austria, pp 267–281
165. Goshtasby A, O'Neill WD (1993) Surface fitting to scattered data by a sum of Gaussians. Comput Aided Geomet Des 10(2):143–156
166. Schagen IP (1980) The use of stochastic processes in interpolation and approximation. Int J Comput Math 8:63–76, Section B
167. Franke R (1982) Scattered data interpolation: tests of some methods. J Math Comput 38(157):181–200
168. Powell MJD (1987) Radial basis functions for multivariate interpolation: a review. In: Cox MG, Mason JC (eds) Algorithms for approximation. Clarendon Press, Oxford, UK, pp 143–167
169. Wendland H (1995) Piecewise polynomial, positive definite and compactly supported radial functions of minimal degree. Adv Comput Math 4:389–396
170. Fornefett M, Rohr K, Stiehl HS (1999) Elastic registration of medical images using radial basis functions with compact support. In: Proceedings of the IEEE computer society conference on computer vision and pattern recognition (CVPR'99), Fort Collins, CO, June 1999, vol 1. pp 402–407
171. Fornefett M, Rohr K, Stiehl HS (2001) Radial basis functions with compact support for elastic registration of medical images. Image Vis Comput 19(1–2):87–96

172. El-Baz A, Farag A, Yuksel S, Abou El-Ghar M, Eldiasty T, Ghoneim M (2007) Application of deformable models for the detection of acute renal rejection. In: Suri JS, Farag A (eds) Handbook of parametric and geometric deformable models: biomedical and clinical applications, vol. II. Springer, New York, pp 293–333, Chapter 10
173. Khalifa F, El-Baz A, Gimel'farb G, Abu El-Ghar M (2010) Non-invasive image-based approach for early detection of acute renal rejection. In: T Jiang et al. (eds): MICCAI 2010, Part I, LNCS 6361, Springer-Verlag, Berlin pp 10–18
174. Nelder JA, Mead R (1965) A simplex method for function minimization. Comput J 7(4):308–313
175. Brent RP (1973) Algorithms for minimization without derivatives. Prentice-Hall, Englewood Cliffs, NJ
176. Levenberg K (1944) A method for the solution of certain non-linear problems in least squares. Q Appl Math 2(2):164–168
177. Shanno DF (1970) Conditioning of quasi-Newton methods for function minimization. Math Comput 24(111):647–656
178. Bernon JL, Boudousq V, Rohmer JF, Fourcade M, Zanca M, Rossi M, Goulart DM (2001) A comparative study of Powell's and Downhill Simplex algorithms for a fast multimodal surface matching in brain imaging. Comput Med Imaging Graph 25(4):287–297
179. Pluim JPW, Maintz JBA, Viergever MA (2001) Mutual information matching in multi-resolution contexts. Image Vis Comput 19(1–2):45–52
180. Jenkinson M, Smith S (2001) A global optimization method for robust affine registration of brain images. Med Image Anal 5(2):143–156
181. Maes F, Vandermeulen D, Suetens P (1999) Comparative evaluation of multiresolution optimization strategies for multimodality image registration by maximization of mutual information. Med Image Anal 3(4):373–386
182. Rohlfing T, Maurer CR Jr, Bluemke DA, Jacobs MA (2003) Volume-preserving nonrigid registration of MR breast images using free-form deformation with an incompressibility constraint. IEEE Trans Med Imaging 22(6):730–741
183. Staring M, Klein S, Pluim JPW (2007) A rigidity penalty term for nonrigid registration. Med Phys 34(11):4098–4108
184. Michalewicz Z (1999) Genetic algorithms + data Structures = evolution programs, 3rd edn. Springer, New York
185. MP Wachowiak, AS Elmaghraby (2001) The continuous Tabu search as an optimizer for 2-D-to-3-D biomedical image registration. In: W Niessen, M Viergever (eds) Lecture notes in computer science, Springer-Verlag, New York, Proc. MICCAI 2001, pp 1273–1274
186. Klein S, Staring M, Pluim JPW (2007) Evaluation of optimization methods for nonrigid medical image registration using mutual information and B-splines. IEEE Trans Image Process 16(12):2879–2890
187. Thévenaz P, Ruttimann UE, Unser M (1995) Iterative multiscale registration without landmarks. In: Proceedings of the IEEE international conference on image processing (ICIP'95), Washington, DC, October 1995, vol 3. pp 228–231
188. Wolberg G, Zokai S (2000) Image registration for perspective deformation recovery. In: Proceedings of the SPIE 14th annual international symposium aerospace, defense sensing, simulation, and controls, Orlando, FL, April 2000, pp 259–270
189. Starink JPP, Baker E (1995) Finding point correspondence using simulated annealing. Pattern Recognit 28(2):231–240
190. Jacq J, Roux C (1995) Registration of non-segmented images using a genetic algorithm. In: Proceedings of the 1st international conference on computer vision, virtual reality and robotics in medicine, April 1995, pp 205–211
191. Thévenaz P, Blu T, Unser M (2000) Image interpolation and resampling. In: Bankman IN (ed) Handbook of medical imaging, processing, and analysis. Academic, San Diego, pp 393–420
192. Unser M (1999) Splines: A perfect fit for signal and image processing. IEEE Signal Process Mag 16(6):22–38

193. Hou HS, Andrews HC (1978) Cubic splines for image interpolation and digital filtering. IEEE Trans Acoust Speech Signal Process 26(6):508–517
194. Unser M, Aldroubi A, Eden M (1993) B-spline signal processing. Part I :theory. IEEE Trans Signal Process 41(2):821–832
195. Hajnal JB, Saeed N, Soar EJ, Oatridge A, Young IR, Bydder GM (1995) A registration and interpolation procedure for subvoxel matching of serially acquired MR images. J Comput Assist Tomogr 19(2):289–296
196. Thacker NA, Jackson A, Moriarty D, Vokurka E (1999) Improved quality of re-sliced MR images using re-normalized sinc interpolation. J Magn Reson Imaging 10(4):582–588
197. Goshtasby AA (2005) 2-D and 3-D image registration for medical, remote sensing, and industrial applications. Wiley, New York
198. Appledorn CR (1996) A new approach to the interpolation of sampled data. IEEE Trans Med Imag 15(3):369–376
199. Dyn N, Levin D, Rippa S (1986) Numerical procedures for global surface fitting of scattered data by radial functions. SIAM J Sci Stat Comput 7:639–659
200. Roche A, Malandain G, Ayache N (2000) Unifying maximum likelihood approaches in medical image registration. Int J Imaging Sys Technol 11(1):71–80
201. Likar B, Pernus F (2001) A hierarchical approach to elastic registration based on mutual information. Image Vis Comput 19(1–2):33–44
202. Musse O, Heitz F, Armspach J (2001) Topology preserving deformable image matching using constrained hierarchical parametric models. IEEE Trans Image Process 10 (7):1081–1093
203. Cain SC, Hayat MM, Armstrong EE (2001) Projection-based image registration in the presence of fixed-pattern noise. IEEE Trans Image Process 10(12):1860–1872
204. Kaneko S, Murase I, Igarashi S (2002) Robust image registration by increment sign correlation. Pattern Recognit 35(10):2223–2234
205. Kaneko S, Satoh Y, Igarashi S (2003) Using selective correlation coefficient for robust image registration. Pattern Recognit 36(5):1165–1173
206. Liu J, Vemuri BC, Marroquin JL (2002) Local frequency representations for robust multimodal image registration. IEEE Trans Med Imaging 21(5):462–469
207. Liu J, Vemuri BC, Bova F (2000) Multi-modal image registration using local frequency. In: Proceedings of the 5th IEEE Workshop Application Computer Vision, Palm Springs, CA, December 2000, pp 120–125
208. Elbakary M, Sundareshan MK (2005) Accurate representation of local frequency using a computationally efficient Gabor filter fusion approach with application to image registration. Pattern Recognit Lett 26(14):2164–2173
209. Vemuri BC, Ye J, Chen Y, Leonard CM (2003) Image registration via level-set motion: applications to atlas-based segmentation. Med Image Anal 7(1):1–20
210. Bertalmio M, Sapiro G, Randall G (2000) Morphing active contours. IEEE Trans Pattern Anal Mach Intell 22(7):733–736
211. Duay V, Houhou N, Thiran JP (2005) Atlas-based segmentation of medical images locally constrained by level sets. In: Proceedings of the IEEE international conference on image processing (ICIP'05), September 2005, vol 2. pp 1286–1289
212. Osher S, Sethian JA (1988) Fronts propagating with curvature-dependent speed – algorithms based on Hamilton-Jacobi formulations. J Comput Phys 79(1):12–49
213. Noblet V, Heinrich C, Heitz F, Armspach JP (2005) 3-D deformable image registration: a topology preservation scheme based on hierarchical deformation models and interval analysis optimization. IEEE Trans Image Process 14(5):553–556
214. Jaulin L, Kieffer M, Didrit O, Walter E (2001) Applied interval analysis. Springer, New York
215. Thévenaz P, Unser M (2000) Optimization of mutual information for multiresolution image registration. IEEE Trans Image Process 9(12):2083–2099
216. Kybic J, Unser M (2003) Fast parametric elastic image registration. IEEE Trans Image Process 12(11):1427–1442

217. Penney G, Batchelor P, Hill D, Hawkes D (2001) Validation of a two- to three-dimensional registration algorithm for aligning preoperative CT images and intraoperative fluoroscopy images. Med Phys 28(6):1024–1032
218. Hipwell JH, Penney GP, McLaughlin RA, Rhode K, Summers P, Cox TC, Byrne JV, Noble JA, Hawkes DJ (2003) Intensity-based 2-D–3-D registration of cerebral angiograms. IEEE Trans Med Imaging 22(11):1417–1426
219. Byrne J, Colominas C, Hipwell J, Cox T, Noble JA, Penney GP, Hawkes DJ (2004) Assessment of a technique for 2-D-3-D registration of cerebral intra-arterial angiography. Br J Radiol 77(914):123–128
220. Sabuncu MR, Ramadge PJ (2003) Spatial information in entropy-based image registration. In: Proceedings of the International Workshop Biomedical Image Registration, Philadelphia, PA, July 2003 (Lecture notes in computer science), vol 2717/2003. Springer, Berlin, pp 132–141
221. Markelj P, Tomazevic D, Likar B, Pernus F (2010) A review of 3-D/2-D registration methods for image-guided interventions. Med Image Anal. http://www.medicalimageanalysisjouranl.com/articles/S1361-8415(10)00036-8/abstract
222. Xie Z, Farin GE (2004) Image registration using hierarchical B-splines. IEEE Trans Vis Comput Graph 10(1):85–94
223. Mora M, Tauber C, Batatia H (2006) 2-D local heart motion estimation using level sets and hierarchical B-splines. In: Proceedings of the 33rd international annual conference on computers in cardiology, Valencia, Spain, September 2006, pp 513–516
224. Tustison NJ, Avants BA, Gee JC (2007) Improved FFD B-spline image registration. In: Proceedings of the IEEE 11th International Conference on Computer Vision (ICCV'07), Rio de Janeiro, Brazil, October 2007, pp 1–8
225. Tustison NJ, Avants BB, Gee JC (2009) Directly manipulated free-form deformation image registration. IEEE Trans Image Process 18(3):624–635
226. Matsopoulos GK, Asvestas PA, Mouravliansky NA, Delibasis KK (2004) Multimodal registration of retinal images using self organizing maps. IEEE Trans Med Imaging 23(12):1557–1573
227. Kim J, Fessler JA (2004) Intensity-based image registration using robust correlation coefficients. IEEE Trans Med Imaging 23(11):1430–1444
228. Wachowiak MP, Peters TM (2006) High-performance medical image registration using new optimization techniques. IEEE Trans Inf Technol Biomed 10(2):334–353
229. Jones DR, Perttunen CD, Stuckman BE (1993) Lipschitzian optimization without the Lipschitz constant. J Optim Theory Appl 79(1):157–181
230. Kolda TG, Lewis RM, Torczon V (2003) Optimization by direct search: New perspectives on some classical and modern methods. SIAM Rev 45(3):385–482
231. Torczon V (1991) On the convergence of the multidirectional search algorithm. SIAM J Optim 1:123–145
232. Lee S, Choi M, Kim H, Park FC (2007) Geometric direct search algorithms for image registration. IEEE Trans Image Process 16(9):2215–2224
233. Orchard J (2007) Efficient least squares multimodal registration with a globally exhaustive alignment search. IEEE Trans Image Process 16(10):2526–2534
234. Sdika M (2008) A fast nonrigid image registration with constraints on the Jacobian using large scale constrained optimization. IEEE Trans Med Imaging 27(2):271–281
235. Glocker B, Komodakis N, Tziritas G, Navab N, Paragios N (2008) Dense image registration through MRFs and efficient linear programming. Med Image Anal 12(6):731–741
236. Slomka PJ, Mandel J, Downey D, Fenster A (2001) Evaluation of voxel-based registration of 3-d power Doppler ultrasound and 3-d magnetic resonance angiographic images of carotid arteries. Ultrasound Med Biol 27(7):945–955
237. Fei B, Zhang S, Savado O, Suri J, Lewin JS, Wilson DL. Three-dimensional automatic volume registration of carotid MR images. In: Proceedings of the 25th annual IEEE

engineering in medicine biology society international conference, September 2003, vol 1, pp 646–648

238. Chan RC, Sokka S, Hinton D, Houser S, Manzke R, Hanekamp A, Reddy VY, Kaazempur-Mofrad MR, Rasche V (2006) Non-rigid registration for fusion of carotid vascular ultrasound and MRI volumetric datasets. Proc SPIE Med Imaging Image Process 6144(2):61442E.1–61442E.8
239. Krucker JF, LeCarpentier GL, Fowlkes JB, Carson PL (2002) Rapid elastic image registration for 3-D ultrasound. IEEE Trans Med Imaging 21(11):1384–1394
240. Nanayakkara ND, Chiu B, Samani A, Spence JD, Samarabandu J, Fenster A (2008) A twisting and bending model-based nonrigid image registration technique for 3-D ultrasound carotid images. IEEE Trans Med Imaging 27(10):1378–1388
241. Sabuncu MR, Ramadge P (2008) Using spanning graphs for efficient image registration. IEEE Trans Image Process 17(5):788–797
242. Staring M, van der Heide UA, Klein S, Viergever MA, Pluim JPW (2009) Registration of cervical MRI using multifeature mutual information. IEEE Trans Med Imaging 28 (9):1412–1421
243. Klein S, Pluim JPW, Staring M, Viergever MA (2009) Adaptive stochastic gradient descent optimization for image registration. Int J Comput Vis 81(3):227–239
244. Loeckx D, Slagmolen P, Maes F, Vandermeulen D, Suetens P (2010) Nonrigid image registration using conditional mutual information. IEEE Trans Med Imaging 29(1):19–29
245. Studholme C, Drapaca C, Iordanova B, Cardenas V (2006) Deformation-based mapping of volume change from serial brain MRI in the presence of local tissue contrast change. IEEE Trans Med Imaging 25(5):626–639

Biography

Fahmi Khalifa received his B.Sc. and M.S. degrees in electrical engineering from Mansoura University, Mansoura, Egypt, in 2003 and 2007, respectively. In May 2009, he joined the BioImaging Laboratory at University of Louisville, Louisville, KY, USA, as a research assistance. His current research is focused on simultaneous image segmentation and registration with main focus on *Automatic Diagnosis of Lung Cancer using Contrast Enhancement Computed Tomography Images*.

Garth M. Beache is an associate professor of radiology, at the University of Louisville School of Medicine, ~~Louisville Kentucky,~~ He completed a fellowship in magnetic resonance research at Massachusetts General Hospital, Harvard Medical School, and has served on the faculty of Johns Hopkins School of Medicine. His research interests include advanced radiological imaging methods, including registration, and functional visualization methods.

Georgy Gimel'farb graduated from Kiev Polytechnic Institute, Kiev, Ukraine, and received the Ph.D. degree in engineering cybernetics from the Institute of Cybernetics, Academy of Sciences of the Ukraine, and the D.Sc. (Eng) degree in control in engineering from the Higher Certifying Commission of the USSR, Moscow, Russia. He joined the University of Auckland, Auckland, New Zealand, in July 1997. His research is focused on image analysis, computer vision, and statistical pattern recognition.

Jasjit S. Suri is an innovator, scientist, a visionary, an industrialist, and an internationally known world leader in Biomedical Engineering. Dr. Suri has spent over 20 years in the field of biomedical engineering/devices and its management. He received his Doctorate from University of Washington, Seattle and Business Management Sciences from Weatherhead, Case Western Reserve University, Cleveland, Ohio. Dr. Suri was crowned with President's Gold medal in 1980 and the Fellow of American Institute of Medical and Biological Engineering for his outstanding contributions.

This figure will be printed in b/w

Ayman El-Baz received the B.Sc. and M.S. degrees in electrical engineering from Mansoura University, Egypt, in 1997 and 2000, respectively, and the Ph.D. degree in electrical engineering from University of Louisville, Louisville, KY. He joined the Bioengineering department, University of Louisville, in August 2006. His current research is focused on developing new computer-assisted diagnosis systems for different diseases and brain disorders